

EUMETSAT Satellite Application Facility on Climate Monitoring

The EUMETSAT
Network of
Satellite Application
Facilities



Algorithm Theoretical Basis Document

HOAPS release 3.2

Near Surface Specific Humidity
Near Surface Wind Speed
Latent Heat Flux
Precipitation
Evaporation
Freshwater Flux

CM-141 (NSH_HOAPS)
CM-142 (SWS_HOAPS)
CM-143 (LHF_HOAPS)
CM-144 (PRE_HOAPS)
CM-145 (EVA_HOAPS)
CM-146 (EMP_HOAPS)

Reference Number:



SAF/CM/DWD/ATBD/HOAPS

Issue/Revision Index:

1.1

Date:

25.03.2011

 	EUMETSAT SAF on CLIMATE MONITORING Algorithm Theoretical Basis Document HOAPS release 3.2	Doc.No.: SAF/CM/DWD/ATBD/HOAPS Issue: 1.1 Date: 25.03.2011
---	--	--

Document Signature Table

	Name	Function	Signature	Date
Author	Axel Andersson	HOAPS Team scientist		12/11/2010
Author	Karsten Fennig Marc Schröder	CM SAF scientist		25/03/2011
Editor	Rainer Hollmann	Science Coordinator		29/03/2011
Approval	Rainer Hollmann	Science Coordinator		29/03/2011
Release	Martin Werscheck	Project Manager		

Distribution List

Internal Distribution	
Name	No. Copies
DWD Archive	1
CM SAF Team	1

External Distribution		
Company	Name	No. Copies
PUBLIC		1

Document Change Record

Issue/ Revision	Date	DCN No.	Changed Pages/Paragraphs
1.0	12/11/2010	SAF/CM/DWD/ATBD/HOAPS/1	First official version.
1.1	25/03/2011	SAF/CM/DWD/ATBD/HOAPS/1	Changes DRI-4





 	EUMETSAT SAF on CLIMATE MONITORING Algorithm Theoretical Basis Document HOAPS release 3.2	Doc.No.: SAF/CM/DWD/ATBD/HOAPS Issue: 1.1 Date: 25.03.2011
---	--	--

Table of Contents



List of Figures.....	4
List of Tables	5
1 The EUMETSAT SAF on Climate Monitoring	6
2 Introduction	6
2.1 Applicable documents	7
2.2 Reference documents	7
3 Processing chain of HOAPS SSM/I and AVHRR Data sources	8
3.1 Product definitions	8
3.2 Data sources and processing	9
3.2.1 The SSM/I Instrument	9
3.2.2 Data processing	10
3.2.3 SSM/I Instrument Homogenization.....	11
3.2.4 Synthesis of 85 GHz channel data	11
3.2.5 Land mask and sea ice detection.....	12
4 Auxiliary data sets	12
4.1 Sea surface temperature	12
4.2 Sea surface saturation specific air humidity	14
5 HOAPS Retrieval Schemes and Parameterizations	14
5.1 Near surface specific humidity (CM-141)	16
5.1.1 Algorithm Description	17
5.1.2 Assumptions and Limitations	20
5.2 Near surface wind speed (CM-142)	20
5.2.1 Algorithm Description	22
5.2.2 Assumptions and Limitations	24
5.3 Turbulent Heat Flux Parameterization and Evaporation (CM-143, CM-145)	25
5.3.1 Background on similarity relationships and flux algorithms	26
5.3.2 Algorithm Description	28
5.3.3 Assumptions and Limitations	30
5.4 Precipitation (CM-144)	31
5.4.1 Algorithm Description	31
5.4.2 Precipitation Neural Network Algorithm.....	31
5.4.3 Assumptions and Limitations	34
5.5 Freshwater flux (CM-146)	35
5.5.1 Assumptions and Limitations	35

 	EUMETSAT SAF on CLIMATE MONITORING Algorithm Theoretical Basis Document HOAPS release 3.2	Doc.No.: SAF/CM/DWD/ATBD/HOAPS Issue: 1.1 Date: 25.03.2011
---	--	--

6	References.....	36
7	Glossary.....	40

List of Figures

Figure 1: Flow chart for the original data processing chain in HOAPS from SSM/I antenna temperatures to geophysical products. Within CM SAF monthly mean products (HOAPS-G) and 6-hourly composites (HOAPS-C) are generated.	8
Figure 2: Temporal coverage of SSM/I instrument aboard DMSP satellite platforms for the HOAPS processing.....	9
Figure 3: Local Equator crossing times of the DMSP satellites.	10
Figure 4: Flow chart for the retrieval scheme of geophysical parameters.....	15
Figure 5: Normalised weighting functions for (a) a mid-latitude atmosphere, and (b) a tropical atmosphere for the SSM/I frequencies. (from Schulz et al., 1993).....	16
Figure 6: Mean water vapour weighting functions for 542 globally distributed atmospheric situations for the lower three SSM/I frequencies. (from Schulz et al., 1993).....	17
Figure 7: Correlation of near-surface specific humidity with water vapour contents in thick layers. The depth of each layer extends from the surface to a height z. (from Schulz et al., 1993)	18
Figure 8: Comparisons between specific air humidity estimated from ship (COADS) measurements and from merged satellite observations during fall, winter, spring, and summer seasons from Oct 1996 to September 1997. (from Bentamy et al., 2003)	19
Figure 9: Simulated variation of SSM/I brightness temperatures with wind speed for a latitude summer situation (from Schlüssel and Luthardt, 1991).....	21
Figure 10: Simulated brightness temperature differences $T_{37v} - T_{37h}$ for 281 globally distributed ocean-atmosphere situations (from Schlüssel and Luthardt, 1991).	22
Figure 11: Neural network architecture of the wind speed retrieval.....	23
Figure 12: Comparison of the HOAPS-3 neural network wind speed retrieval (black), the algorithms of Schlüssel and Luthardt (1991) (red) and Stogryn et al. (1994) (blue) against the verification data set of the neural network algorithm. The verification data set contains wind speed measurements	

 	EUMETSAT SAF on CLIMATE MONITORING Algorithm Theoretical Basis Document HOAPS release 3.2	Doc.No.: SAF/CM/DWD/ATBD/HOAPS Issue: 1.1 Date: 25.03.2011
---	--	--

from buoys and radiosonde measurements. The latter are binned in 2 m/s steps, resulting in discrete intervals for higher wind speeds..... 24



Figure 13: Neural network architecture of the precipitation retrieval algorithm. (from Andersson et al., 2010) 32

Figure 14: Comparison of different precipitation algorithms. (a) shows the retrieved precipitation rates of the neural network algorithm (black), the Bauer and Schlüssel (1993) algorithm (red) and the Ferraro (1997) algorithm (blue) against the precipitation rates from the verification data set. (b) shows the accumulated histogram of precipitation as the fraction of total precipitation for the different retrievals and the verification data set between 0.2 mm/h and 30 mm/h. (from Andersson, 2010) 34

List of Tables

Table 1: NOAA satellite IDs for AVHRR instruments used in NODC/RSMAS Pathfinder V5. (i) denotes periods with interim coefficients. 13

Table 2: Accuracies of the neural net algorithm for precipitation. N = number of samples; mean, bias, and RMS are in mm/h. (see text) 33

 	EUMETSAT SAF on CLIMATE MONITORING Algorithm Theoretical Basis Document HOAPS release 3.2	Doc.No.: SAF/CM/DWD/ATBD/HOAPS Issue: 1.1 Date: 25.03.2011
---	--	--

1 The EUMETSAT SAF on Climate Monitoring

The importance of climate monitoring with satellites was recognized in 1999 by EUMETSAT Member States when they amended the EUMETSAT Convention to affirm that the EUMETSAT mandate is also to contribute to the operational monitoring of climate and the detection of global climatic changes". Following this, EUMETSAT established within its Satellite Application Facility (SAF) network a dedicated centre, the SAF on Climate Monitoring (CM SAF, <http://www.cmsaf.eu>). Since the start of the CM SAF in 1999 the project went through three phases, i.e., the Development Phase lasting from 1999 to 2004, the Initial Operations Phase (IOP) and the Continued Development and Operations Phase (CDOP). The consortium of CM SAF currently comprises the Deutscher Wetterdienst (DWD) as host institute, and the partners from the Royal Meteorological Institute of Belgium (RMIB), the Finnish Meteorological Institute (FMI), the Royal Meteorological Institute of the Netherlands (KNMI), the Swedish Meteorological and Hydrological Institute (SMHI) and the Meteorological Service of Switzerland (MeteoSwiss).

After focusing on the development of retrieval schemes to derive a subset of Essential Climate Variables (ECVs) in the development phase, CM SAF delivered to its users products based on Meteosat and polar orbiter data for Europe and Northern Africa supporting NMHSs in their provision of climate services in the IOP from 2004 to 2007. During CDOP, lasting from 2007 to 2012, the product validation continued, the time series were expanded and algorithms were further improved, while the study domain was extended from the baseline area to the MSG disk for the geostationary products and to include global and Arctic coverage for the polar orbiter products. In addition, long term climate datasets from polar orbiting and geostationary satellites are being generated for climate monitoring (i.e. HOAPS, METEOSAT and AVHRR-GAC based products).



A catalogue of available CM SAF products is available via the CM SAF webpage, <http://www.cmsaf.eu/>. Here, detailed information about product ordering, add-on tools, sample programs and documentation are provided.

2 Introduction

This CM SAF Algorithm Theoretical Basis Document (ATBD) provides information on the processing chain implemented for the HOAPS data set to retrieve geophysical parameters from homogenized SSM/I observations and auxiliary information from AVHRR SST retrievals. It also provides information on the CM SAF retrieval schemes used to construct the data set employing Special Sensor Microwave/Imager (SSM/I) observations onboard Defence Meteorological Satellite Program (DMSP) platforms F08, F10, F11, F13, F14 and F15. The same algorithms have already been used in the Hamburg Ocean-Atmosphere Parameters and fluxes from Satellite (HOAPS, <http://www.hoaps.org/>) data set (Andersson et al. 2010). The document gives background information on the physics of the problem, the training and derivation of the statistical inversion schemes and consideration of constraints and limitations of the retrievals. It is based on the description of the HOAPS data set by Andersson et al. 2010.

At first a description of the data sources and processing chain, including a summary of instrument characteristics, are given, followed by an introduction to the homogenization method for the SSM/I radiometers, and the parameter retrieval scheme design.

More information on the data set is contained in the product user manual [RD 2], basic accuracy requirements are defined in the product requirements document [RD 1], and the

 	EUMETSAT SAF on CLIMATE MONITORING Algorithm Theoretical Basis Document HOAPS release 3.2	Doc.No.: SAF/CM/DWD/ATBD/HOAPS Issue: 1.1 Date: 25.03.2011
---	--	--

validation of the data set versus those requirements is described in the validation report [RD 3].

The HOAPS data set contains multiple parameters derived from SSM/I observations. The CM SAF release of HOAPS 3.2 contains the following atmospheric and near-surface variables, derived for the global ice-free oceans:

Near surface specific humidity [CM-141, NSH_HOAPS, section 5.1],

Wind speed at 10m height [CM-142, SWS_HOAPS, section 5.2],

Latent heat flux at sea surface [CM-143, LHF_HOAPS, section 5.3],

Evaporation [CM-145, EVA_HOAPS, section 5.3],

Precipitation [CM-144, PRE_HOAPS, section 5.4],

Freshwater flux [CM-146, EMP_HOAPS, section 5.5].

2.1 Applicable documents

Reference	Title	Code
AD 1	Memorandum of Understanding between CM SAF and the Max-Planck Institute for Meteorology and Meteorological Institute, University of Hamburg	
AD 2	Cooperation Agreement	

2.2 Reference documents

Reference	Title	Code
RD 1	CM SAF Product Requirements Document	SAF/CM/DWD/PRD/1.6
RD 2	Product User Manual	SAF/CM/PUM/HOAPS/1.1
RD 3	Validation Report	SAF/CM/VAL/HOAPS/1.1

3 Processing chain of HOAPS SSM/I and AVHRR Data sources

This section provides information on the processing chain implemented for the HOAPS data set to retrieve geophysical parameters from homogenized SSM/I observations and auxiliary information from AVHRR SST retrievals.

3.1 Product definitions

The CM SAF HOAPS data set from SSM/I provides quasi-global coverage over the ice-free ocean surface, i.e., within $\pm 180^\circ$ longitude and $\pm 80^\circ$ latitude. Instantaneous SSM/I retrievals at original swath level are used to derive the spatio-temporal averaged data sets. The products are available as 6-hourly composites and monthly averages on a regular latitude/longitude grid with a spatial resolution of $0.5^\circ \times 0.5^\circ$ degrees. The temporal coverage of the data sets ranges from 9th of July 1987 to 31st of December 2008. More detailed information on the

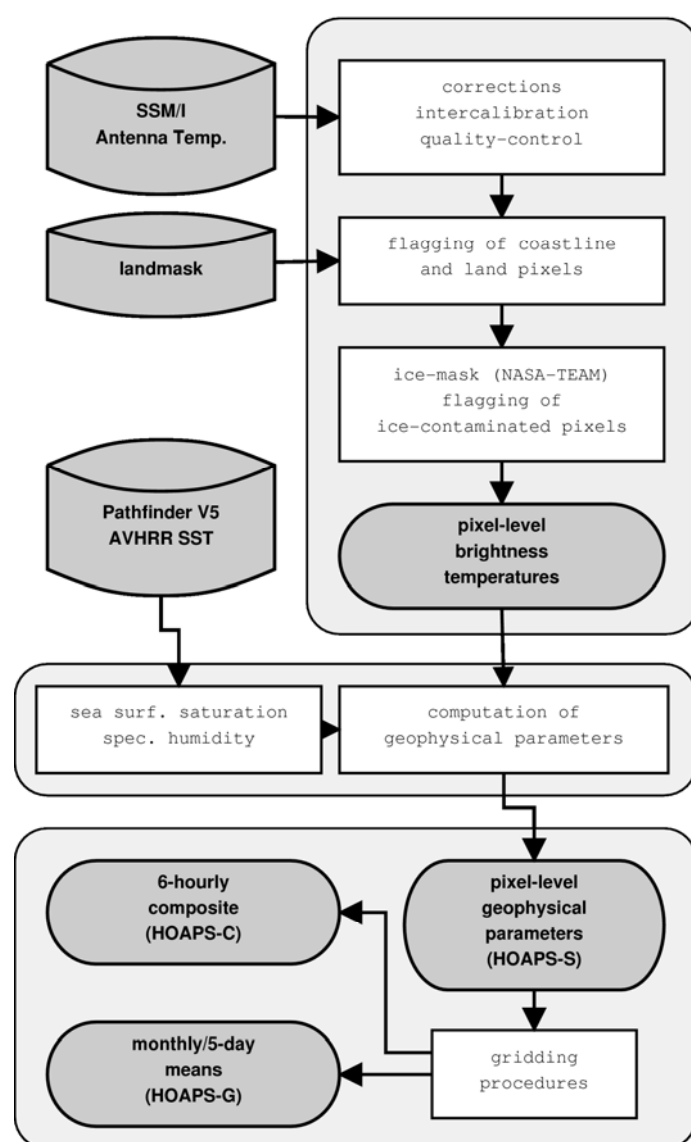



Figure 1: Flow chart for the original data processing chain in HOAPS from SSM/I antenna temperatures to geophysical products. Within CM SAF monthly mean products (HOAPS-G) and 6-hourly composites (HOAPS-C) are generated.

	EUMETSAT SAF on CLIMATE MONITORING Algorithm Theoretical Basis Document HOAPS release 3.2	Doc.No.: SAF/CM/DWD/ATBD/HOAPS Issue: 1.1 Date: 25.03.2011
---	--	--

products and data format specifications are given in the Product User Manual [RD 2].

3.2 Data sources and processing

The starting point in the data processing chain, as illustrated in Figure 1 are SSM/I antenna temperatures. These are converted to an internal brightness temperature (TB) data set. This procedure includes several instrument-related corrections, inter-sensor calibration, and the flagging of land and sea ice covered pixels. From the TB data set and the NODC/RSMAS Pathfinder SST, geophysical parameters are calculated on the native SSM/I resolution (HOAPS-S). Finally, the previously described gridded HOAPS products are generated from the scan-based HOAPS-S data.

3.2.1 The SSM/I Instrument

SSM/I sensors have been carried aboard the DMSP satellite series since 1987. Up to three radiometers have been in orbit simultaneously, as shown in Figure 2. An extensive description of the instrument and satellite characteristics has been published by Hollinger (1990) and Wentz (1991). Hence, only a very short summary of essential information is given here. The DMSP satellites fly in a near-circular, sun-synchronous orbit, with an inclination of 98.8° at an approximate altitude of 860 km. Each day, 14.1 orbits with a period of about 102 min are performed. The Earth's surface is sampled with a conical scan at a constant local zenith angle of 53.1° and a 1400 km wide swath. A nearly complete coverage of the Earth by one SSM/I is achieved within two to three days. Due to the orbit inclination and swath width, the regions poleward of 87.5° are not covered. To date, six SSM/I instruments have been successfully launched aboard the F08, F10, F11, F13, F14 and F15 spacecraft. All satellites have a local equator crossing time between 5 and 10 A.M./P.M. for the descending/ascending node. The F08 had a reversed orbit with the ascending node in the morning. Also, the Earth observing portion of the scan on this satellite is, differently from the others, centred to the aft. Most of the DMSP satellites have a very stable orbit as shown in Figure 3. The temporal variation of the equator crossing times is less than three hours for all satellites. At the end of the HOAPS-3 time period the orbits of F14 and F15 begin to decay noticeably, but are still within 2-3 hours of original time.

The SSM/I is a seven channel total power radiometer measuring emitted microwave radiation at four frequency intervals centred at 19.35, 22.235, 37.0, and 85.5 GHz. All frequencies are sampled at horizontal and vertical polarization, except for the 22.235 GHz channel, which measures only vertically polarized radiation. The channels will be referred to as 19, 22, 37, and 85 GHz hereafter and the corresponding brightness temperatures of each channel and polarization as TB19v/h, TB22v, TB37v/h, and TB85v/h.

The spatial resolution varies from 69 km by 43 km with a sampling frequency of 25 km for the 19 GHz channel to 15 km by 13 km with 12.5 km sampling frequency for the 85 GHz

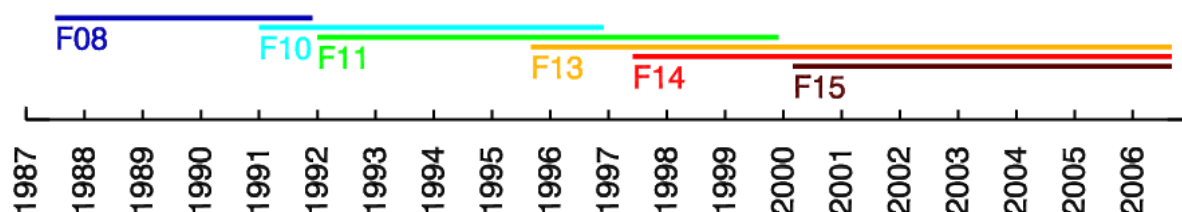


Figure 2: Temporal coverage of SSM/I instrument aboard DMSP satellite platforms for the HOAPS processing.

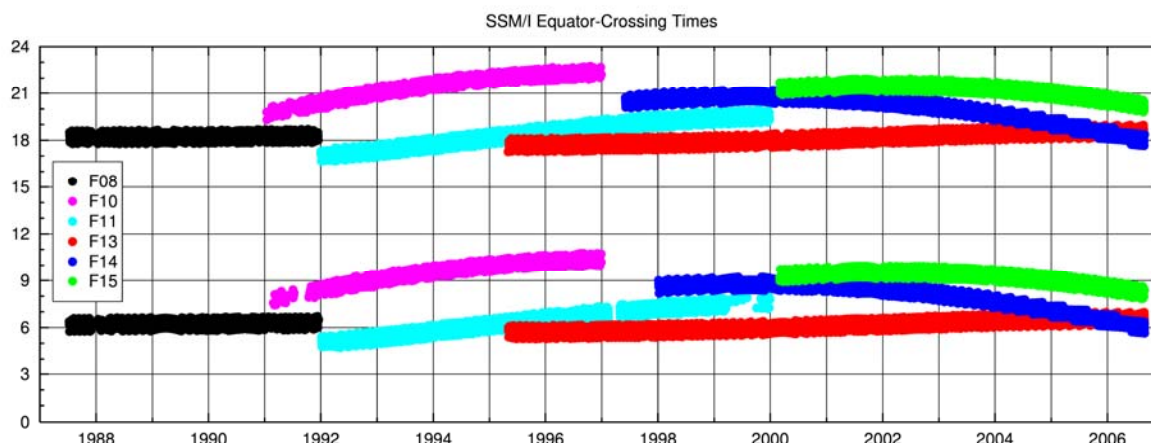


Figure 3: Local Equator crossing times of the DMSF satellites.


channel. The 85 GHz channels are sampled for each rotation of the instrument (A and B-scans) with a resolution of 128 uniformly spaced pixels, while the remaining channels are sampled every other scan (A-scans) with a resolution of 64 pixels. A fixed cold space reflector and a reference black body hot load are used for continuous onboard two point calibration.

3.2.2 Data processing

Antenna Temperature Tapes (ATT) from Remote Sensing Systems (RSS) as well as Temperature Data Records (TDR) from the National Environmental Satellite, Data, and Information System (NESDIS), NOAA's Satellite and Information Service, are used as SSM/I input data for HOAPS. Either data source has been used during several time periods for various logistic reasons. An analysis of SSM/I data from different sources (Ritchie et al., 1998), including NESDIS TDR and RSS ATT data, showed no systematic differences between these data sets.

In a first step the different input data sets are pre-processed into a common internal data format containing navigated and calibrated antenna temperatures. The antenna temperatures are then converted to TBs according to Wentz (1991) using a fixed set of antenna pattern corrections. In addition, this procedure treats several known issues with the radiometer, including corrections for an along-scan bias (Wentz, 1991; Colton and Poe, 1999) and zenith angle variations (Furhop and Simmer, 1996). The correction coefficients for the along-scan correction have been updated and the along-scan correction is applied to all SSM/I channels. The normalisation of the brightness temperature to a fixed zenith angle using the Furhop and Simmer method is not available for the 85 GHz channels and thus a statistical linear correction is applied instead.

For the application of the retrieval algorithms it is important that about the same area is seen by all channels. Due to the higher frequency, a single field of view (FOV) at 85 GHz covers only about 18% of the area sampled at 37 GHz (cf. e.g. Spencer et al., 1989). Since the 85 GHz channels are sampled twice as often in each direction compared to all other SSM/I channels, nine neighbouring 85 GHz pixels of the A and B-Scans are averaged down to the resolution of the corresponding 37 GHz pixel. The 85 GHz pixels are averaged with their Gaussian weighted distance from the centre FOV analogue to the 37 GHz antenna pattern.

	EUMETSAT SAF on CLIMATE MONITORING Algorithm Theoretical Basis Document HOAPS release 3.2	Doc.No.: SAF/CM/DWD/ATBD/HOAPS Issue: 1.1 Date: 25.03.2011
---	--	--

3.2.3 SSM/I Instrument Homogenization

In order to ensure a homogeneous time series of the successive SSM/Is, the slightly varying individual instrument characteristics have to be corrected by an inter-sensor calibration of the radiometers. The calibration procedure is based on the SSM/I on DMSP F11 which is selected as the reference for a relative intercalibration. In tests with different wind speed algorithms against in-situ buoy data this radiometer exhibits a reliable long-term stability. Furthermore it has a temporal overlap with most of the other radiometers. The SSM/Is on F08 and F15, which do not have a temporal overlap with F11, are calibrated to the F10 and F13 radiometers, respectively. The inter-calibration method used is an updated version of the homogenization scheme described in Andersson et al. (2010).

The calibration coefficients are determined by linear regression from match-up data sets of the radiometers that are based on the TBs after the along-scan bias correction and zenith angle normalization. The match-up data sets are constructed from oceanic TBs of each channel that are binned into daily global 1° by 1° grid, separately for ascending and descending orbits. For each radiometer a match-up data set with the selected reference radiometer is compiled from the collocated gridded mean TBs for at least one overlapping year. The calibration coefficients are then calculated by a least squares linear regression between the TB pairs of both radiometers, separately for ascending and descending orbits and then averaged to minimize the influence of diurnal cycle variations.



Due to the accurate and stable in-orbit calibration of the SSM/I, the coefficients are considered to be constant during the lifetime of a radiometer (Colton and Poe, 1999) and are used to homogenize the measurements of different SSM/I instruments. However, the unstable and highly elliptical DMSP F10 orbit could lead to second order effects on the internal calibration which are not covered by the intercalibration match-up method and made a recalibration for the radiometer aboard this satellite necessary. The F10 calibration coefficients were determined for the years 1992 and 1996 and then linearly interpolated for the intermediate years.

3.2.4 Synthesis of 85 GHz channel data

Due to thermal problems, the SSM/I on the DMSP F08 had to be switched off in December 1987. When the radiometer was reactivated, the 85 GHz vertical polarization channel exhibited significantly increased noise levels. Later, similar problems occurred with the 85 GHz horizontal polarization channel (Hollinger, 1990; Wentz, 1992; Ferraro, 1997). Therefore, the 85 GHz channels of the SSM/I on DMSP F08 are regarded as defective from April 1988 until the end of the lifetime of the radiometer and the respective original SSM/I data is not used in HOAPS.

This failure affects all HOAPS parameters depending on these channel, in particular the precipitation retrieval. A computationally efficient way of handling this problem is to synthesize approximate values of the missing 85 GHz information from the remaining channels. The synthesis is based on a neural network approach, which is used to estimate TB 85v/h of the 9-pixel averaged 85 GHz FOV from the other SSM/I channels (TB 19v/h, TB22v, and TB37v/h). The training data set for the neural network was compiled from randomly selected brightness temperatures of SSM/I radiometers on board DMSP F11, F13, and F14 from 1998. More details on the 85 GHz synthesis algorithm are given in Andersson et al. (2010).

The synthesis allows the application of the same retrieval algorithms for all parameters throughout all analysis steps without individual replacement algorithms for each affected

 	EUMETSAT SAF on CLIMATE MONITORING Algorithm Theoretical Basis Document HOAPS release 3.2	Doc.No.: SAF/CM/DWD/ATBD/HOAPS Issue: 1.1 Date: 25.03.2011
---	--	--

parameter. It has, however, to be kept in mind that such a procedure cannot fully reconstruct the specific 85 GHz information but is a computationally convenient way of handling the missing data by a plausible replacement. Moreover, this method is only valid over open water. Over land surfaces this general approach is not applicable due to the strongly varying surface emissivity.

3.2.5 Land mask and sea ice detection

For SSM/I pixels within 50 km of any coastline and sea ice margin no geophysical parameters are derived in HOAPS. This is to avoid any contamination of the data by the abrupt change in surface emissivity between water and land or sea ice covered areas, respectively. The corresponding areas are flagged during the processing in the pixel-level data (see Figure 1).

The land-sea mask is derived from the Global Land One-km Base Elevation data base (GLOBE, 1999). This data set is further adjusted by first removing small islands and landmasses with a diameter of less than 5 km, treating these areas as open water. In a second step the coastlines of the remaining land areas are expanded 50 km into the sea.

To account for the varying sea ice margins, a daily sea ice mask is compiled from the HOAPS SSM/I TBs. These maps are created in two steps. First the total sea ice covered fraction within a single SSM/I FOV is computed using the NASA Team sea ice algorithm of Swift (1985). The resulting sea ice observations from all available SSM/I instruments are then gridded to common daily mean fields on a regular $0.5^\circ \times 0.5^\circ$ grid. In order to distinguish between short-lived strong rain events and persisting sea ice, which are characterized by similar TB signatures, only grid boxes with an average sea ice fraction above 15% for at least 5 consecutive days are flagged as ice covered. Daily sea ice maps are then derived from this reduced data set by re-expanding the reliably identified sea ice areas in time and space and filling remaining data gaps by spatial and temporal interpolation. Finally, the resulting sea ice margin is extended 50 km into the ocean to avoid any spurious sea ice signal in the HOAPS retrievals.

4 Auxiliary data sets

4.1 Sea surface temperature

To exclusively rely on satellite data for the computation of latent and sensible heat flux parameters, the NOAA National Oceanographic Data Center (NODC) and Miami's Rosenstiel School of Marine and Atmospheric Science (RSMAS) Oceans Pathfinder Version 5.0 SST (Kilpatrick, 2001; Casey, 2004; NODC, 2008) product is used within HOAPS.

In the Pathfinder data set a quality flag with a value from 0 to 7 is assigned for each pixel, with 7 being the highest quality observation. For the further processing in HOAPS, only pixels with an overall quality flag of four or higher are accepted. This conforms to the Pathfinder Version 4 "best-SST" product and involves several quality checks including a cloud screening (c.f. Kilpatrick (2001) for details).

The Pathfinder data set consists of data from several AVHRRs, one at a time. Table 1 shows the individual NOAA satellites and their temporal coverage in the NODC/RSMAS Pathfinder V5 as used for HOAPS-3. Periods denoted with (i) refer to a year of data where interim coefficients from the previous year are used to calculate empirical coefficients in the Pathfinder SST algorithm. At the time of the processing of HOAPS-3, Pathfinder SST data computed with regular coefficients were not available for these periods and data based on the interim coefficients is used. The regular coefficients are computed from a buoy match-up data

set and are processed with a delay to the real-time data in order to maintain the long term stability of the data set (NODC, 2008). Consequently, the SST values computed using the interim coefficients may reveal a slight bias compared to the final data which are released later.

The Pathfinder algorithm coefficients are determined by a regression of the measured ocean skin infrared brightness temperatures against buoy data (Kilpatrick, 2001), which means the derived SST technically represents a sub-skin SST with the mean sub-skin minus skin SST difference (cold skin effect) removed. However, the mean daytime Pathfinder SST is found to be roughly 0.1 K colder than in-situ SST and the night-time SST is about 0.3 K colder (Reynolds, 2002). The reason for this cold bias is unclear, but is most likely caused by undetected clouds. For most regions the value of this cold bias has roughly the same magnitude as the cool skin effect. Hence, the Pathfinder SST is treated as a skin SST for the surface flux calculations in HOAPS.

The AVHRR Pathfinder day and night-time observations are averaged to daily mean SST maps with a grid resolution of 0.25°.

In regions that are covered by clouds, no SST data is available, as such pixels are rejected by the quality control. Hence, the data void regions are filled by spatial and temporal interpolation. The interpolation procedure is as follows:

- interpolation in time: look for a value up to 10 days forth in time and then up to 10 days back in time. If two valid SST values are found within this time period the missing data is linearly interpolated.
- Gaussian weighted spatial interpolation: at first try to interpolate with a radius of 100 km and then with 300 km maximum distance.

Some grid boxes may remain unfilled, e.g. due to persistent cloud cover.



Finally, the data is remapped to native SSM/I pixel resolution. The SST value for each SSM/I pixel is selected from the daily map by the centre position of the respective FOV.

In the wake of the volcanic eruption of Mt. Pinatubo in June 1991 the high load of volcanic aerosol contaminated the AVHRR radiance measurements. Undetected aerosol leads to a night-time cold bias in the daily mean SST fields (Reynolds, 1993). During the first phase for about 6 months following the eruption a significant bias is introduced in the SST. This affects the retrievals of latent and sensible heat flux in HOAPS. In 1992 the effect weakens, but may persist until 1993. However, for the decaying phase we consider the signal not to be entirely

Table 1: NOAA satellite IDs for AVHRR instruments used in NODC/RSMAS Pathfinder V5.

(i) denotes periods with interim coefficients.

Year	Satellite
1987–1988	NOAA-09
1989–1994	NOAA-11
1995–2000	NOAA-14
2000–2002	NOAA-16
2003–2005	NOAA-17
2005–2006	NOAA-18
2007–2008	NOAA-18 (i)

 	EUMETSAT SAF on CLIMATE MONITORING Algorithm Theoretical Basis Document HOAPS release 3.2	Doc.No.: SAF/CM/DWD/ATBD/HOAPS Issue: 1.1 Date: 25.03.2011
---	--	--

spurious since an analogous response with a decay time of up to 31 months after the eruption is independently observed in global tropospheric temperatures and water vapour data (Soden, 2002; Harries, 2006).

4.2 Sea surface saturation specific air humidity

For the derivation of the evaporation through the bulk formula, the difference in humidity, i.e. sea surface specific humidity minus near surface specific humidity, is calculated. The sea surface saturation specific air humidity is calculated by applying the Magnus formula to the Pathfinder V5 SST input data:

$$e_w = 6.1078 \exp \left[\frac{a(T - 273.16)}{T - b} \right] \quad (1)$$

Where e_w is in [hPa], T is temperature in [K], $a = 17.2693882$, $b = 35.86$ (Murray, 1967).

An approximate salinity correction to take into account the reduction in vapour pressure caused by a typical salinity of 34 parts per thousand is applied by scaling the value for pure water with a factor of 0.98 (Sverdrup et al., 1942):

$$e_{w_sal} = 0.98 \cdot e_w \quad (2)$$

$$q_s = (0.622099 * e_{w_sal} / (slp - 0.377901 \cdot e_{w_sal})) \quad (3)$$

where q_s is the saturation specific humidity in [kg/kg]; slp is the sea-level pressure, which is implemented with a constant value of 1013.25 hPa.

The q_s values are calculated individually for each SST observation prior to the gridding and remapping procedures which are the same as for the SST (see above).

5 HOAPS Retrieval Schemes and Parameterizations

In the following the retrieval schemes to derive HOAPS parameters are described. All parameters are derived from SSM/I measurements. The latent heat flux is estimated using a bulk aerodynamic approach employing Fairall et al. (1996b, 2003). This method requires the knowledge of near surface wind speed, atmospheric near surface specific humidity, and the SST. The latter is derived from AVHRR measurements.

All retrievals are implemented on the SSM/I pixel level data, i.e. are derived for each valid SSM/I field of view. Internally the processing is done for each SSM/I scan line with a loop over the 64 individual scan positions. Figure 4 shows a flow chart of the geophysical parameter retrieval. In the first step land, coasts, and ice covered regions are excluded, followed by several threshold test to identify erroneous measurements and to skip the corresponding pixel.

The precipitation is derived next using the neural network algorithm (c.f. section 5.4) followed by the wind speed (c.f. section 5.2). If the retrieval of the wind speed is not possible due to high liquid water content or high rain water content, all remaining parameters are also skipped. Atmospheric columnar water vapour and the near surface specific humidity (c.f. section 5.1) are the next parameters that are retrieved.

If water vapour values greater than 80 g/kg are derived, the brightness temperatures are assumed to be erroneous. The pixel is set to undefined for all parameters and the loop is continued with the next pixel.

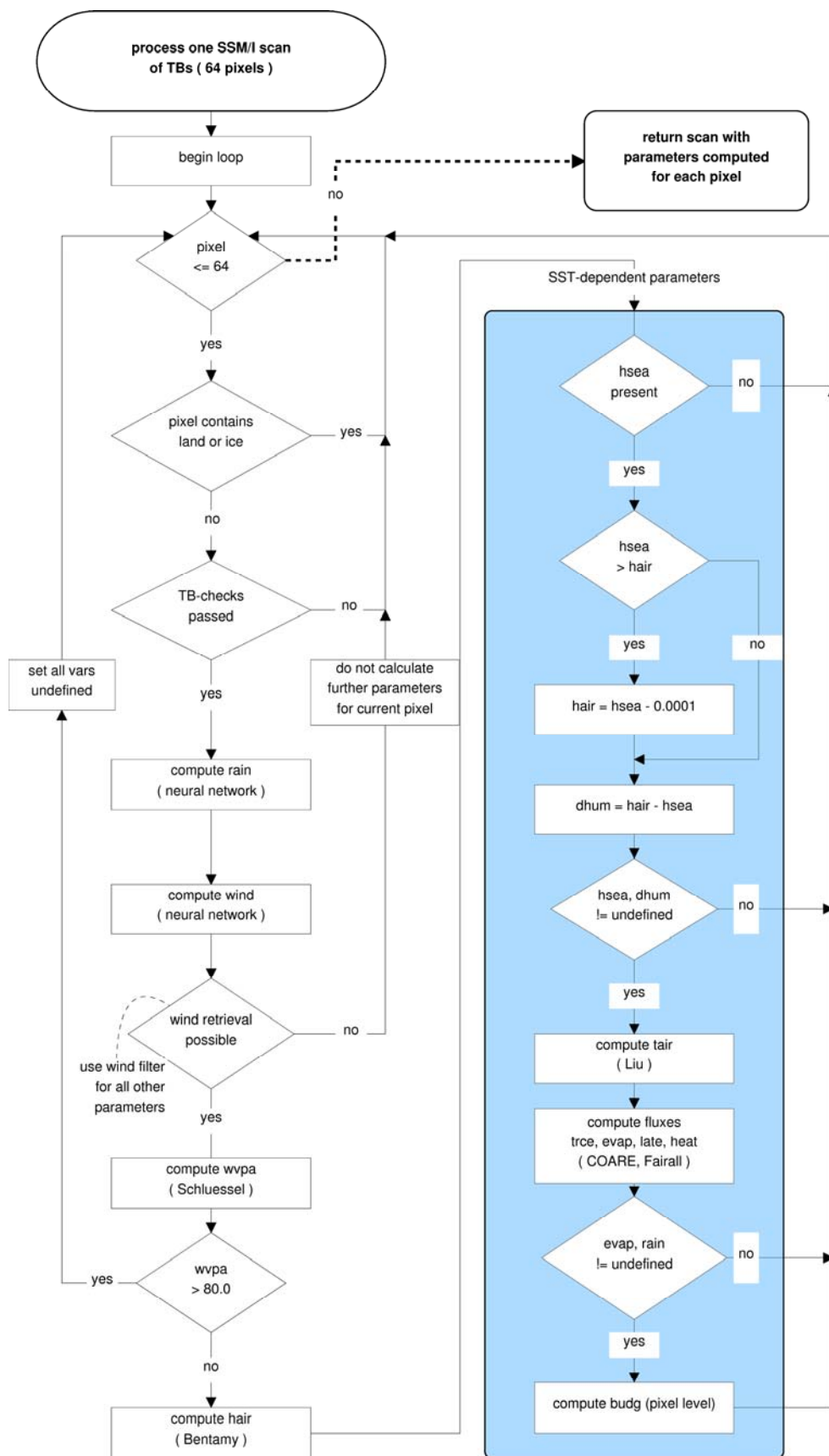


Figure 4: Flow chart for the retrieval scheme of geophysical parameters

The computation of the turbulent fluxes depends on the SST, which is remapped from AVHRR Pathfinder data to the SSM/I pixels (c.f. section 4) and is only continued if valid sea surface temperature and saturation specific humidity values are present.

If precipitation (c.f. section 5.4) and evaporation (c.f. section 5.3) are retrieved the freshwater flux is computed. This is only the case for situations with no or very light rain. However, for the gridded mean products the freshwater flux is computed as the difference of the individual averages of the evaporation and precipitation parameters (c.f. section 5.5).

5.1 Near surface specific humidity (CM-141)

A direct measurement of the humidity in the layer directly above the sea surface from satellite soundings is difficult to obtain. Radiometers, such as the SSM/I, measure the radiation that originates from a relatively thick layer rather than from a single level. However, the satellite-retrieved signal contains some information to derive the humidity in the lowermost layer of the boundary layer.

On climatological scale the near surface specific humidity, q_a is highly correlated with the total columnar water vapour (Liu, 1986). Since the water vapour content can be reliably derived from SSM/I brightness temperatures this relationship could be used to derive q_a using the retrieved water vapour as a proxy. Although this method provides a reasonable estimate on the global monthly and climatological scale, it is not suitable to derive values of q_a on regional scale or for individual scenes. This is especially the case when the planetary boundary layer is decoupled from the upper troposphere (Schlüssel, 1989).

The algorithm that is applied here directly relates SSM/I brightness temperatures to q_a instead of deriving q_a from SSM/I-derived water vapour estimates. A multi-linear relationship from Bentamy (2003) is used, which is based on the two-step retrieval of Schulz (1993) and the refinement of Schlüssel (1995). It derives q_a directly from SSM/I brightness temperatures using the 19 GHz, 22 GHz, and 37 GHz channels.

An additional advantage of this multi-channel approach is the possibility of a better separation

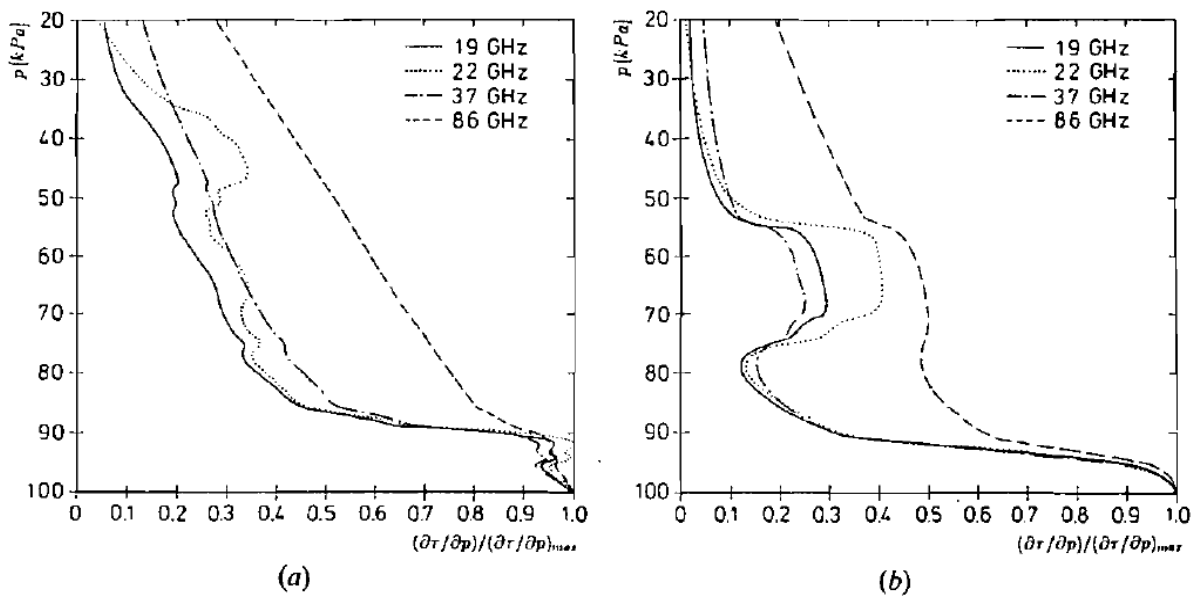


Figure 5: Normalised weighting functions for (a) a mid-latitude atmosphere, and (b) a tropical atmosphere for the SSM/I frequencies. (from Schulz et al., 1993)

of wind induced surface signals from the water vapour signal through the 19 and 37 GHz channels, which reduces the errors in the retrieval.

5.1.1 Algorithm Description

Because the 22 GHz SSM/I channel is centred on a water vapour absorption line, it is suitable to retrieve the atmospheric water vapour content. However, the signal from this channel is only appropriate to derive the total columnar water vapour. To retrieve the water vapour in the lower part of the boundary layer, additional information is needed.

In order to assess the sensitivity of SSM/I measurements to variations of the near-surface humidity, Schulz et al. (1993) compiled a data set of 542 radiosonde and surface in situ data from several field experiments. The data set contains profiles from all seasons and tropical as well as mid to high latitudes. Using this data base, radiative transfer calculations were set up to simulate SSM/I radiometer signals.

Figure 5 shows the result from the radiative transfer calculations for the weighting functions of the SSM/I frequencies as determined by Schulz et al. (1993). The profiles were obtained for two clear atmospheric cases from a mid-latitude (Figure 5a) and a tropical (Figure 5b) radiosonde profile. The different channels are normalized with their absolute maximum for better comparability. It is clearly evident that the weighting functions strongly decrease with height and a significant signal from the lowermost 500 m of the boundary layer is contained in the radiation measured by the SSM/I. This indicates, that the SSM/I measurements are sufficiently sensitive to the bottom-layer-integrated water vapour in particular using the 19, 22, and 37 GHz vertical and 19 GHz horizontal polarization measurements.

The absolute maxima of the profiles are located in the atmospheric boundary layer close to the surface. Since the secondary maximum in the 22 GHz channel between 70 and 50 kPa is more expressed especially for the tropical case, the 19 and 37GHz measurement have to be considered primarily for the derivation of q_a .

A second important factor is the sensitivity of the brightness temperatures to changes in water

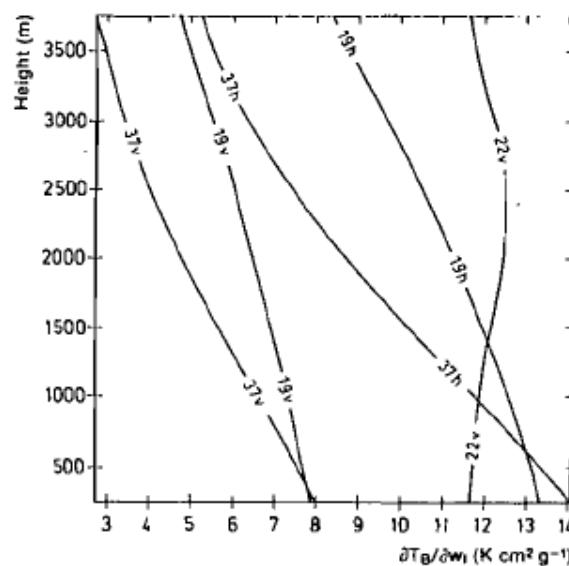


Figure 6: Mean water vapour weighting functions for 542 globally distributed atmospheric situations for the lower three SSM/I frequencies. (from Schulz et al., 1993)

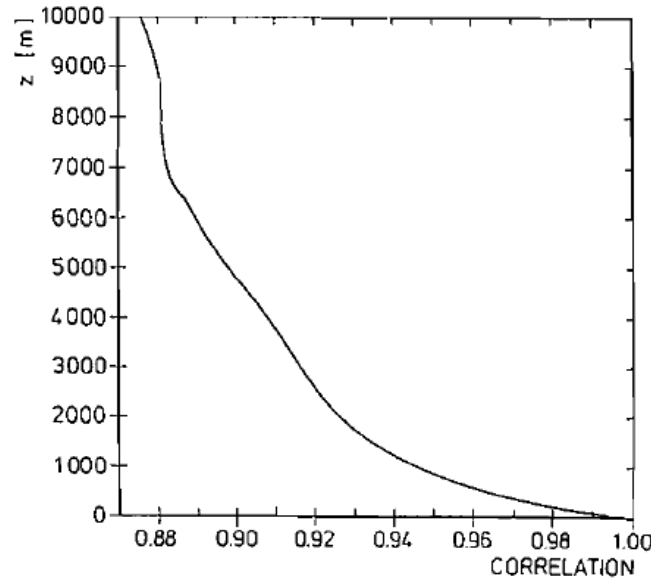


Figure 7: Correlation of near-surface specific humidity with water vapour contents in thick layers. The depth of each layer extends from the surface to a height z .
(from Schulz et al., 1993)

vapour contents in different atmospheric layers, $\partial T_B / \partial w_i$, as it is shown in Figure 6. The mean weighting functions were calculated for 500 m thick layers below 4 km from the same simulation data base as above (Schulz et. al., 1993).

While a well pronounced decrease of $\partial T_B / \partial w_i$ with height is detectable in the 19 and 37 GHz channels, the 22 GHz channel exhibits a nearly uniform response over all height levels. The maximum sensitivity for the 19 and 37 GHz channels is located in the lowest level with a stronger decrease at 37 GHz than at 19 GHz, again indicating the presence of a lower boundary layer water vapour signal in these channels.

However, the correlation of a single channel with the water vapour signal from the lowermost 500 m of the boundary layer is too weak for a single channel retrieval. Hence, a multichannel retrieval has to be used. An additional advantage of using the 19 and 37 GHz channels is the possibility to make the algorithm sensitive for wind induced surface signals and hence to reduce the errors in the retrieval.

Based on the above findings, Schulz et al. (1993) derived a linear retrieval equation for the water vapour content (w_l) in the lowermost 500 m, using a multivariate regression analysis with a subset of the 542 simulations.

This resulted in a retrieval of the form:

$$w_l = a_0 + a_1 \cdot T_{19V} + a_2 \cdot T_{19H} + a_3 \cdot T_{22V} + a_4 \cdot T_{37V} \quad (4)$$

In a second step the lower boundary layer water vapour content can be linearly related to q_a . Figure 7 shows the correlation between near-surface specific humidity and water vapour contents for layers with increasing depth derived from the radiosonde data set. High correlations greater than 0.9 are evident for a layer thickness of up to 3,000 m. For a layer of 500 m depth the correlation is 0.96. This assumption holds true for most situations, since the oceanic atmospheric boundary layer is usually well mixed. This relationship is combined with the lower boundary layer water vapour content retrieval (Eq. 4) in a two step algorithm to

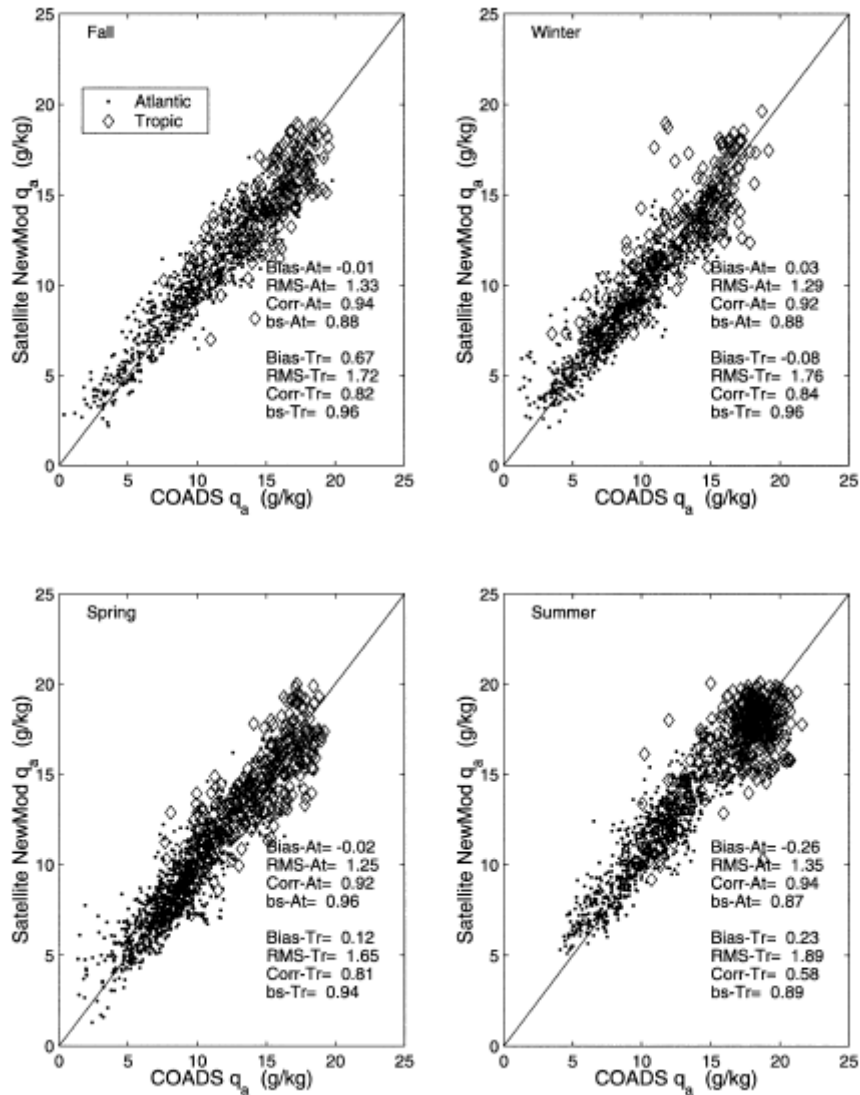




Figure 8: Comparisons between specific air humidity estimated from ship (COADS) measurements and from merged satellite observations during fall, winter, spring, and summer seasons from Oct 1996 to September 1997. (from Bentamy et al., 2003)

relate SSM/I brightness temperatures to q_a . Together with the above retrieval for w_l , q_a is determined by:

$$q_a = -0.53 + 19.49 \cdot w_l \quad (5)$$

Schlüssel et al. (1995) extended the database to 9,445 situations from radiosonde and surface observations and found a correlation of $r=0.968$ between both parameters. The high correlation justifies a direct regression based retrieval of q_a from the SSM/I brightness temperatures instead of the two step approach. Using this assumption and the extended data base an improved version of the Schulz et al. (1993) retrieval was derived and used in HOAPS version 1. However, evaluations by Ataktürk and Katsaros (1998) revealed an overestimation of q_a in tropical regions by these retrievals. A bias of 2 g/kg occurred in the inner tropics due to high total column precipitable water values.

 	EUMETSAT SAF on CLIMATE MONITORING Algorithm Theoretical Basis Document HOAPS release 3.2	Doc.No.: SAF/CM/DWD/ATBD/HOAPS Issue: 1.1 Date: 25.03.2011
---	--	--

Bentamy et al. (2003) showed that the chosen linear channel combination of SSM/I channels is sufficient for the direct estimation of the near surface specific humidity. With a sample of 1,000 pairs from an improved data base of collocated satellite (F10, F11, F13, and F14) and ship data for the period October 1996 to September 1997, the regression coefficients were recalculated to reduce the biases.

The new model and its coefficients are provided by the following equation as used in the current HOAPS retrieval:

$$q_a = a_0 + a_1 \cdot T_{19V} + a_2 \cdot T_{19H} + a_3 \cdot T_{22V} + a_4 \cdot T_{37V} \quad (6)$$

where $a_0 = -55.9227$, $a_1 = 0.4035$, $a_2 = -0.2944$, $a_3 = 0.3511$, and $a_4 = -0.2395$.

Figure 8 shows a comparison of collocated satellite and ship data from Bentamy (2003). The satellite data were calculated using the improved model in Eq. 6. On average, the bias is reduced by 15% compared to the Schulz et al. (1993) model and is no longer statistically significant. The RMS difference between satellite estimate and ship q_a observation is 1.40 g/kg. Over the North Atlantic Ocean, where 80% of ship data are located, the maximum values of the difference between satellite and ship q_a is about 0.25 g/kg and is found during the summer season, where q_a values are high. Although the bias in the tropics is removed, the RMS values are generally higher compared to the North Atlantic values.

5.1.2 Assumptions and Limitations

For atmospheric situations with high liquid water content or high rain water content the retrieval of the near surface specific humidity is not possible, since the strong emission from atmospheric water is masking the signal. Hence a filter for such situations has been implemented using a threshold technique to determine high water content values within the sampled pixel. The respective values are treated as undefined in the data set.

As the implemented retrieval is a statistical procedure, it is only as good as the quality of the input data set. Since the training data for the retrieval originates from ship data, not all regions and hence atmospheric situations may be equally well represented in the training data set. This is for example the case for situations with relatively warm air layer above cold water, as it occurs in upwelling regions, where larger errors in the retrieval may occur.

In scenes over very warm water masses with high air humidity the satellite-retrieved q_a signal tends to saturate. This leads to a tendency to underestimate q_a for values above 20 g/kg.

Another general issue in the training data set is that the buoy data consists of temporal averages of point measurements which are related to area averages of the SSM/I footprint. This introduces additional scatter into the data through the different scales of the data. However, the number of samples in the input data is large enough, to compensate for this.

5.2 Near surface wind speed (CM-142)

The near surface wind speed cannot be measured directly from space. Over the ocean, the effects of the wind friction on the surface alter the emissivity of the ocean surface in the microwave spectrum. Thus the wind speed is dynamically coupled to gravity and capillary waves and foam coverage of the ocean surface, which in turn influences the surface emissivity and hence the upwelling radiances. At satellite altitude, the SSM/I brightness temperatures (especially TB19h and TB37h) increase non-linearly with increasing wind speed (e.g. Webster et.al 1976). Furthermore, TB19v, TB22v, and TB37v have to be considered in order to remove

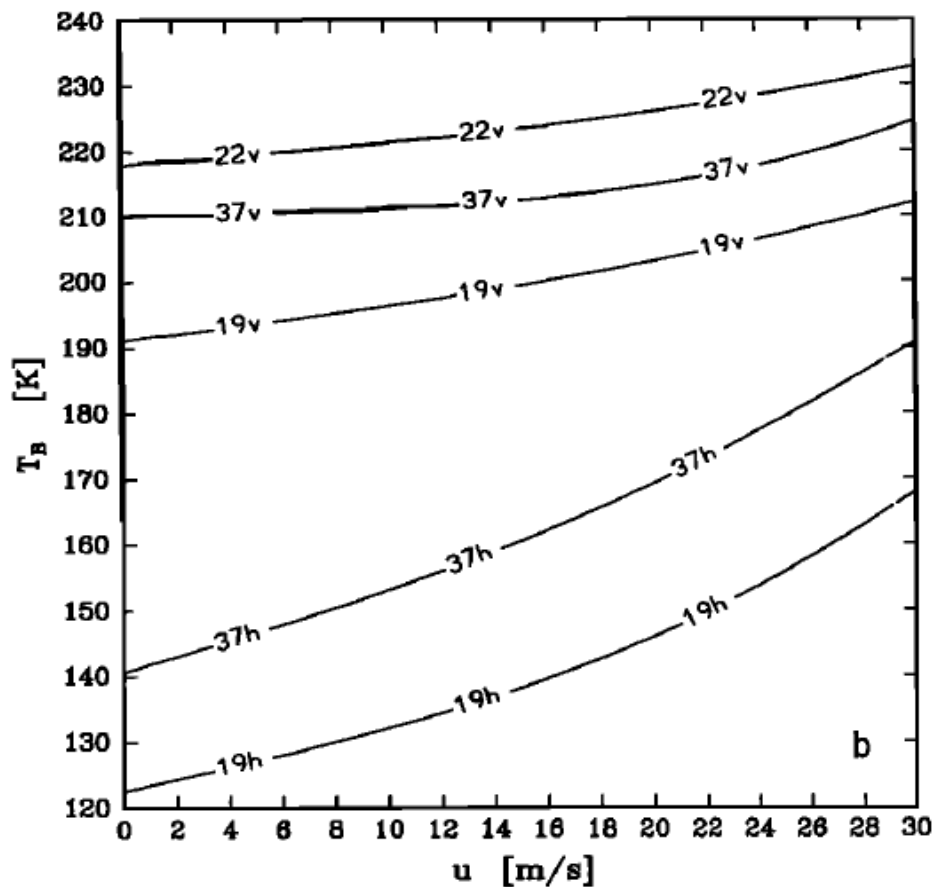


Figure 9: Simulated variation of SSM/I brightness temperatures with wind speed for a latitude summer situation (from Schlüssel and Luthardt, 1991).

the atmospheric contribution to the radiometric signal, which would otherwise tamper the wind induced surface signatures.

Figure 9 shows the dependence of simulated SSM/I brightness temperatures on the wind speed. Especially for the horizontally polarized 37 GHz and 19 GHz channels a strong dependence on the wind speed is evident. The signal for the vertically polarized channels is less pronounced, but also noticeable. With increasing wind speed the polarization differences of the 19 GHz and 37 Hz channels decrease, as is shown in Figure 10 from globally distributed simulations by Schlüssel and Luthardt (1991)

This behaviour has been proven by observations and was used for the derivation of relatively simple linear wind speed algorithms (e.g. Goodberlet, 1989). However, such algorithms do not describe the non-linear evolution of the brightness temperatures very accurately. Physical retrievals or more sophisticated statistical models do allow to account for the non-linearity of the problem and additionally to deal with different atmospheric conditions such as clear sky or cloudy regimes. This is particularly important in situations where the atmospheric moisture increases and the relation of the observed brightness temperatures on the wind speed becomes significantly non-linear (Petty and Katsaros, 1992, 1994). Within the HOAPS data set a statistical neural network based retrieval is used. This approach has shown to result in good performing retrievals (Stogryn et al., 1994; Krasnopolsky et al., 1995).

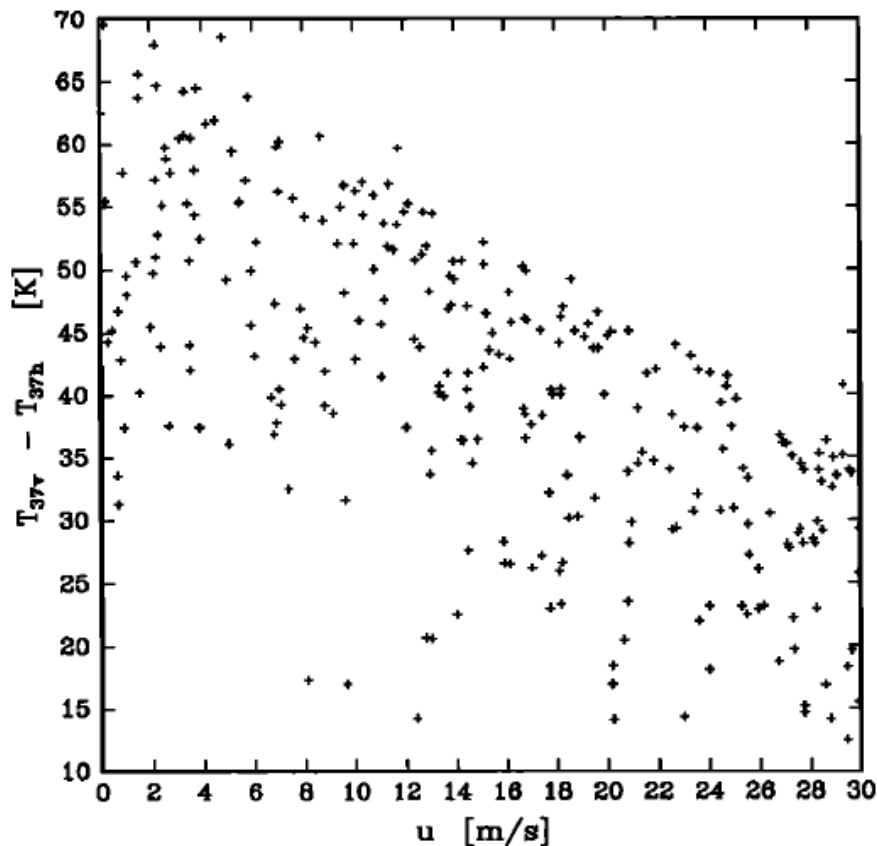


Figure 10: Simulated brightness temperature differences $T_{37v} - T_{37h}$ for 281 globally distributed ocean-atmosphere situations (from Schlüssel and Luthardt, 1991).

5.2.1 Algorithm Description

The HOAPS wind speed algorithm follows a neural network approach after Krasnopolsky et al. (1995). Stogryn et al. (1994) and Krasnopolsky et al. (1995) demonstrated the applicability of neural networks to derive wind retrieval schemes based on SSM/I measurements. These algorithms showed the advantage of being capable to reliably retrieve wind speeds under cloudy conditions, which is important to retrieve information from active weather systems.

Generally, the ocean surface wind speed algorithm relates an input vector P of the measured brightness temperatures to an output vector of the geophysical parameter(s) G through a transfer function f :

$$G = f(P) \quad (7)$$

where the transfer function is determined using a neural network in this case.

Following this approach, the wind speed is estimated using a fully connected 3-layer feed forward neural network, composed of one input layer utilizing TB19v/h, TB22v, and TB37v/h, a hidden layer with three neurons and an output layer with one neuron, the wind speed. All three neurons in the hidden layer are non-linear with the sigmoid function \tanh as the unit's activation function. The output neuron is linear in order to maximize the networks' extrapolation capabilities. The layout of the neural network is shown in Figure 11.

Two different data sets were used to serve as input for the training of the neural network. One is derived from radiosonde profiles and radiative transfer simulations and a second one from

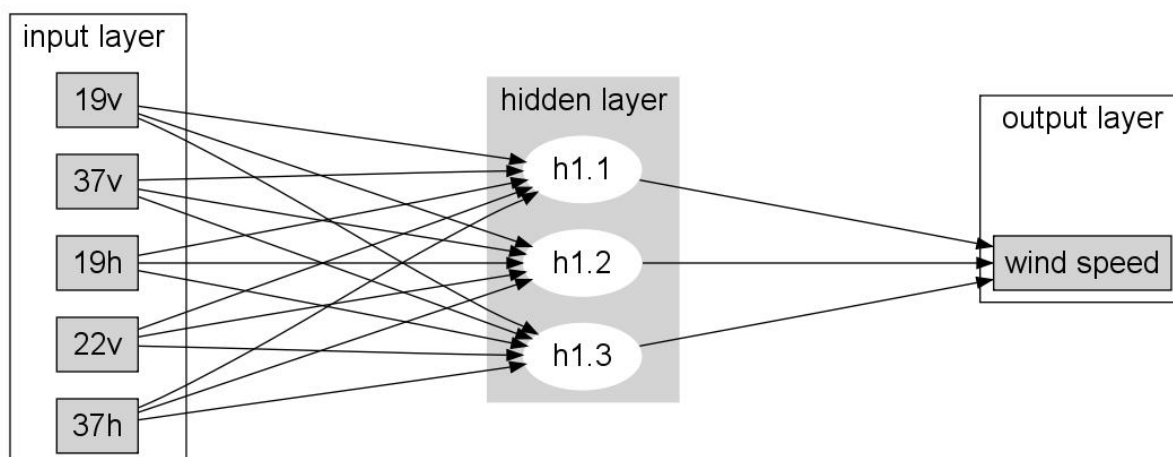


Figure 11: Neural network architecture of the wind speed retrieval.

collocated SSM/I and buoy observations. This approach ensures the representativeness of global input data with a wide range of atmospheric situations of the input and output data of the neural network.

The radiosonde data set consists of about 2,000 globally distributed atmospheric profiles. The near surface wind speed is assigned to each profile at equidistant steps of 2 m/s within a range from 2 to 30 m/s. The radiation emitted from the ocean surface is calculated with the surface emissivity model of Bauer (2001) and the top of the atmosphere radiance is calculated with the radiative transport scheme of Schlüssel and Emery (1990)

The buoy data set is compiled using match-ups between SSM/I F11 brightness temperatures (TBs) with near-surface wind speed measurements from 20 buoys from the National Data Buoy Center (NDBC) and 59 buoys from the Tropical Atmosphere/Ocean (TAO) array for the years 1997 and 1998. The buoy wind speed data represent hourly 8 minute mean values. The criterion of a maximum difference of 30 minutes and 50 km between satellite and buoy observations resulted in a match-up data set of about 470,000 samples for the chosen period. The buoy wind speed measurements were individually converted to a height of 10 m wind using a logarithmic wind profile assuming neutral stratification using the Fairall (1996) scheme.

Both data sets are then combined by collecting all data samples in 2 m/s wide wind speed bins, ensuring that all parts of the wind spectrum are equally weighted. The neural network's training data set is then compiled by taking an equal number of randomized samples from each of the wind speed bins. The resulting data set consists of about 15,000 samples. By taking randomized samples separately for each bin, the input TBs cover the whole possible range of atmospheric conditions including high water vapour observations from the TAO buoys. The lower wind speed ranges are mixed with data samples from both data sets, while most samples larger than 15 m/s originate from the set of radiative transfer calculations.

Figure 12 shows the performance of the wind speed retrieval compared to the algorithms of Schlüssel and Luthardt (1991) and Stogryn et al. (1994). Applied to the verification data set, the neural network wind speed algorithm exhibits a very low bias of -0.02 m/s, a standard deviation of 1.5 m/s, and a correlation coefficient of $r = 0.98$. The standard deviation for the HOAPS neural network algorithm is much lower compared to 4.0 m/s and 5.26 m/s for the two other retrievals.

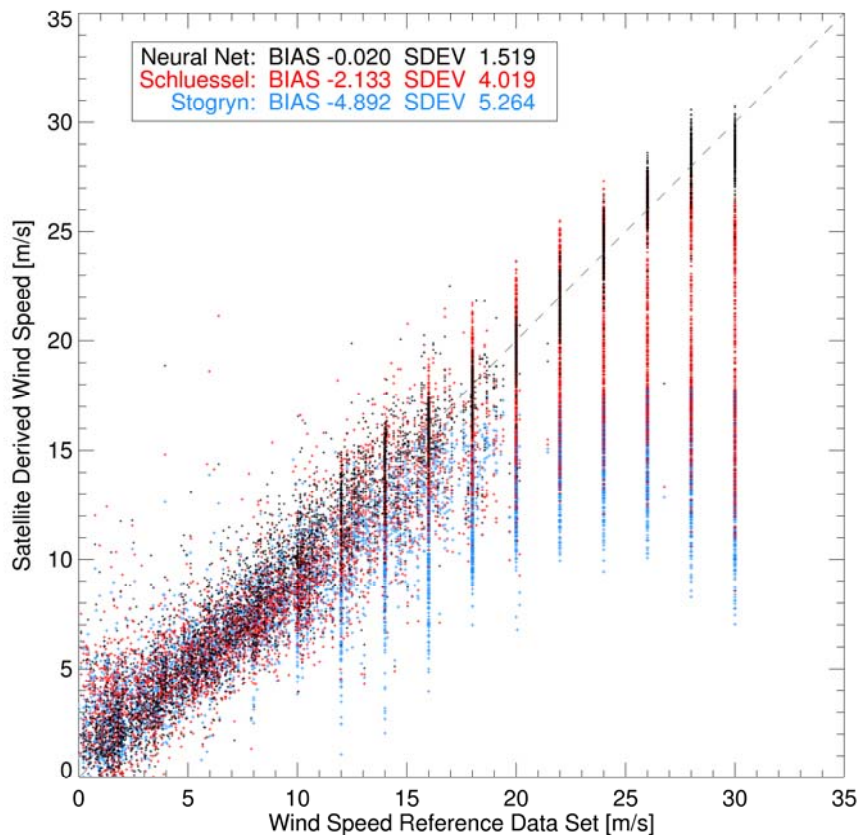



Figure 12: Comparison of the HOAPS-3 neural network wind speed retrieval (black), the algorithms of Schlüssel and Luthardt (1991) (red) and Stogryn et al. (1994) (blue) against the verification data set of the neural network algorithm. The verification data set contains wind speed measurements from buoys and radiosonde measurements. The latter are binned in 2 m/s steps, resulting in discrete intervals for higher wind speeds

When the entire buoy data set is used (not shown) the bias is 0.08 m/s, with a standard deviation of 1.65 m/s and $r = 0.83$. Comparable values were found by Winterfeldt et al. (2010) who compared wind speed from HOAPS, NCEP, and the QuikSCAT/SeaWinds scatterometer with buoy data from the North Sea and North Atlantic. The comparisons for the HOAPS wind speed algorithm showed a mean RMS of 2 m/s for near coastal as well as for open ocean regions.

In contrast to the neural network algorithm the other wind speed retrievals shown in Figure 12 exhibit a strong tendency to saturate at high wind speeds. This results in an overall underestimation with biases of -2.1 m/s for the Schlüssel algorithm and -4.9 m/s for the Stogryn algorithm.

5.2.2 Assumptions and Limitations

For atmospheric situations with high liquid water content or high rain water content the retrieval of the near surface wind speed is not possible, since the strong emission from atmospheric water is masking the signal. Hence a filter for such situations has been

	EUMETSAT SAF on CLIMATE MONITORING Algorithm Theoretical Basis Document HOAPS release 3.2	Doc.No.: SAF/CM/DWD/ATBD/HOAPS Issue: 1.1 Date: 25.03.2011
---	--	--

implemented using a threshold technique to determine high water content values within the sampled pixel.

As the implemented retrieval is a statistical procedure, it is only as good as the quality of the input data set. While the spatial representativeness of the data set is ensured, it is impossible to include every atmospheric situation. Hence, some extreme situations might not be included in the training data set. Here the extrapolation capabilities of the neural network should ensure reasonable retrievals.

Another issue in the training data set is that the buoy data consists of temporal averages of point measurements which are related to area averages of the SSM/I footprint. This introduces additional scatter into the data through the different scales of the data. However, the number of samples in the input data is large enough, to compensate for this.

5.3 Turbulent Heat Flux Parameterization and Evaporation (CM-143, CM-145)

Latent and sensible heat fluxes (Q_l and Q_s , respectively) are an important mechanism in the earth's energy budget, through which about 20% of the total radiation that is absorbed by the earth's surface is transferred back to the atmosphere (Trenberth, 2009). The direct measurement of these fluxes with space borne sensors is not possible. However, they can be estimated from wind speed and sea-air humidity and temperature differences using a bulk aerodynamic approach of the form:

$$Q_l = \rho L_E C_E u (q_s - q_a) \quad (8)$$

and


$$Q_s = \rho c_p C_T u (T_s - \theta_a) \quad (9)$$

where ρ is air density, c_p is specific heat of the air at constant pressure, u is the wind speed at 10 meters height, L_E is the latent heat of evaporation, C_T is the Stanton number, C_E is the Dalton number, T_s is the surface skin temperature (here SST), θ_a is the potential air temperature, q_s is the saturation specific humidity at the sea surface, and, q_a is the specific humidity at the 10 m atmospheric measurement level.

Nearly all of these geophysical parameters needed to derive the fluxes can be retrieved directly or indirectly from satellite observations. As a matter of principle all parameters could be derived from microwave radiometer data, apart from the air temperature and the transfer coefficients C_T and C_E . However, the retrieval of the SST in the infrared spectrum is possible with a higher accuracy than in the microwave spectrum. In HOAPS, the parameterization of the latent and sensible heat transfer coefficients is based on the Coupled Ocean–Atmosphere Response Experiment (COARE) bulk aerodynamic approach of Fairall (1996, 2003). The sensible heat flux is not part of the HOAPS parameters released through the CM SAF.

The following section covers the theoretical background of the parameterization for the latent heat, resp. evaporation, retrieval through the COARE aerodynamic bulk approach. The algorithm itself does not necessarily depend on satellite retrievals. However, the relevant input parameters are obtained from satellite data within HOAPS. For the retrieval of the latent heat flux these are:

- Wind speed at 10 m height (c.f. section 5.2),
- Near surface specific humidity (c.f. section 5.1),
- Sea surface temperature (c.f. section 4.1),
- Sea surface saturation specific humidity (c.f. section 4.2).

	EUMETSAT SAF on CLIMATE MONITORING Algorithm Theoretical Basis Document HOAPS release 3.2	Doc.No.: SAF/CM/DWD/ATBD/HOAPS Issue: 1.1 Date: 25.03.2011
---	--	--

5.3.1 Background on similarity relationships and flux algorithms

In the following a short introduction to the theory behind flux retrievals will be given. More complete information on flux methods can be found in related publications (e.g. Smith et al., 1996 or Fairall et al., 1997).

The conservation equation for the ensemble mean of variable x , denoted as X , is

$$\frac{\partial X}{\partial t} + \nabla_h X \cdot U_h = -\frac{\partial(\overline{w'x'})}{\partial z} + \overline{I_x} \quad (10)$$

where horizontal components are denoted by the subscript h , w' represents the vertical wind fluctuations, and I_x represents the source term.

The Reynolds flux enclosed in parentheses is the quantity, which is of interest for the retrieval. In this case it would be the latent heat flux Q_L .

Several methods can be used to determine this quantity. One possibility is a direct measurement of the spatial or temporal development of w and x and computing their mean product, the so called covariance or eddy-correlation method.

Due to difficulties in making covariance measurements over the ocean on large horizontal and temporal scales with sufficient coverage, a variety of different approaches to make flux measurements have been developed. Additional complications, such as sea spray and salt particles as well as the movement of the measurement platform and disturbances by the equipment require other methods than the direct flux measurements. There are several indirect estimates, such as the inertial-dissipation method or budget methods (e.g. Fairall and Larsen 1986; Edson et al. 1991).

If information with a high temporal and spatial resolution is not available, algorithms have to be applied that rely on the parameterization of the surface using bulk meteorological variables (e.g., surface temperature, surface air temperature, humidity, and wind). These parameters can be measured relatively easy either in situ or remotely.


In HOAPS the COARE bulk flux algorithms are used. These are based on the Monin-Obukhov similarity theory (MOST). The application of MOST to atmospheric parameters is not general, such as covariance methods, but is used to estimate surface fluxes only. Through the bulk formulas turbulent fluxes are derived from mean values of surface meteorological variables such as surface temperature, wind, and surface air temperature and humidity.

The basic approach of MOST is to scale the mean and turbulent properties of the dynamical variables by combinations of surface fluxes, while their height dependence is described by the ratio of the height above the surface to the Monin-Obukhov length L (Fairall, 1997, 2003). MOST is one of the most widely used scaling theories in meteorology and has been applied extensively over the ocean and forms the basis of several surface flux estimation methods. In the following a short introduction to the basics of the COARE algorithms will be given according to Fairall (1996, 2003).

5.3.1.a Bulk scaling theory

The bulk fluxes are derived from mean quantities of basic parameters based on MOST:

$$\overline{w'x'} = c_x^{1/2} c_d^{1/2} S \Delta X = C_x S \Delta X \quad (11)$$

	EUMETSAT SAF on CLIMATE MONITORING Algorithm Theoretical Basis Document HOAPS release 3.2	Doc.No.: SAF/CM/DWD/ATBD/HOAPS Issue: 1.1 Date: 25.03.2011
---	--	--

where x represents parameters such as the wind components u and v , the potential temperature θ , or the water vapour specific humidity, q . c_x and c_d are the bulk transfer coefficients for the variable x and wind speed (here subscript d). C_x is the total transfer coefficient.

ΔX denotes the air-sea difference of the mean value of the variable x :

$$\Delta X = X_{sea} - X(z) \quad (12)$$

The mean wind speed S in Eq. 11 includes the mean U and V components as well as a gustiness part (U_g):

$$S = (U^2 + V^2 + U_g^2)^{1/2} \quad (13)$$

U_g accounts for the sub-grid-scale variability in the wind field and is parameterized depending on the surface stability.

The transfer coefficients in Eq. 11 are also calculated depending on the surface stability. This relationship is given by the MOST:

$$c_x^{1/2}(\zeta) = \frac{c_{xn}^{1/2}}{\left[1 - \frac{c_{xn}^{1/2}}{\kappa} \Psi_x(\zeta) \right]}$$

$$c_{xn}^{1/2} = \frac{\kappa}{\ln(z/z_{0x})} \quad (14)$$

where the subscript n denotes the neutral ($\zeta=0$) stability state with $\Psi_x=0$, Ψ_x is an empirical function in the bulk algorithm that describes the stability dependence of the mean profile, κ is von Karman's constant, z is the height of measurement of the mean quantity $X(z)$, and z_{0x} is the roughness length which characterizes the neutral transfer properties of the surface for the quantity, x .

The MOST stability parameter, $\zeta (= z/L)$, is given by

$$\zeta = -\frac{\kappa g z}{T} \frac{(\overline{w'\theta'} + 0.61T\overline{w'q'})}{(-\overline{w'u'})^{1/2}} \quad (15)$$

where T is the temperature, g the acceleration due to gravity, and $w'u'$ denotes the streamwise component.

For equation 15 the following MOST scaling parameters can be defined for velocity, temperature and humidity:



$$u^* = \sqrt{-\overline{w'u'}}$$

$$\theta^* = -\overline{w'\theta'}/u^*$$

$$q^* = \overline{w'q'}/u^* \quad (16)$$

(u^* is also known as the friction velocity).

These scaling parameters can be computed independently from the transfer coefficient given in Eq. 14 and are obtained by iteration within the bulk algorithm.

 	EUMETSAT SAF on CLIMATE MONITORING Algorithm Theoretical Basis Document HOAPS release 3.2	Doc.No.: SAF/CM/DWD/ATBD/HOAPS Issue: 1.1 Date: 25.03.2011
---	--	--

The equations 11-13 and 15 represent the basis for a bulk flux algorithm. Hence, such a model must contain parameterizations for the roughness lengths (or, equivalently the transfer coefficients) and the empirical profile stability functions Ψ_x .

5.3.2 Algorithm Description

HOAPS-3 latent and sensible heat fluxes are parameterized using the COARE bulk flux algorithm version 2.6a (Bradley et al., 2000), which is an updated version of the COARE 2.5b algorithm (Fairall et al., 1996), based on an extended flux database containing covariance measurements from higher latitudes and under stronger wind conditions. With minor modifications of physics and parameterizations to the version 2.6a, the algorithm is equivalent to the algorithm published as COARE 3.0 by Fairall et al. (2003).

The COARE 3.0 algorithm is derived from more than 5000 direct covariance flux measurements collected over the global oceans. Further updates to the previous version 2.5 were a variable Charnock parameter, a new roughness length parameterization for wind speeds up to 20 m/s, and adjustments to the basic profile stability functions to improve the results under near-stable boundary layer conditions.

The stability dependent MOST scaling parameters (Eq. 16) and wind gustiness U_g (Eq. 13), which accounts for sub-scale variability, are estimated iteratively in the COARE algorithm.

The algorithm is run for each SSM/I pixel where all necessary input data are available. These are:



- wind speed u (c.f. section 5.2)
- near surface specific humidity q_{air} (c.f. section 5.1)
- sea surface saturation specific humidity q_{sea} (derived from SST, c.f. section 4.2)
- skin temperature T_s (SST, c.f. section 4.1)
- air temperature T_{air} (derived from q_{air} and SST, c.f. section 5.3.3)

The implementation of the COARE algorithm in HOAPS omits the warm-layer code, since no continuous diurnal cycle information on the surface radiation budget is available from SSM/I or AVHRR measurements. These are needed to infer the warm layer evolution and cool skin effect. Furthermore, the code for the precipitation flux is also not implemented in the HOAPS retrieval.

The liquid water evaporation equivalent of the latent heat flux is related to the latent heat flux by:

$$E = Q_l / (L_E \rho_0) \quad (17)$$

where ρ_0 is the freshwater density as a function of temperature (Fairall, 1996).

 	EUMETSAT SAF on CLIMATE MONITORING Algorithm Theoretical Basis Document HOAPS release 3.2	Doc.No.: SAF/CM/DWD/ATBD/HOAPS Issue: 1.1 Date: 25.03.2011
---	--	--

The parameterization code is structured as follows (only the parts relevant for the latent heat flux retrieval are shown):

Step 1:

Data input of constant variables.

- Input atmospheric measurement heights. (10m)
- Input inversion height, stratification stability criterion (600m)
- surface pressure (1013.25 hPa)
- Set all predetermined constants (von Karman, etc.)

Main Loop

Step 2:

- Input a line of data from time series: u , T_s , q_{air} , q_{sea}

Step 3:

- Compute first guess transfer coefficients and u^* , T^* , and q^* .
Compute all temperature dependent constants.
- Set loop count to 0

Step 4:

Stability iteration loop (3 iterations):


- Compute parameters:
 - ζ (Eq. 15)
 - z_0 , using wind speed dependent Charnock parameter above 10 m/s
 - neutral transfer coefficients (Eq. 14)
- Compute stability dependence:
 - Ψ function and stability dependent transfer coefficients (Eq.14)
 - if unstable, compute wind gustiness U_g (Eq. 13)
 - θ^* , q^* , u^* (Eq. 16)
 - compute latent heat flux (Eq. 11)
- Increment loop count; if loop count < 3, go to Step 4

Step 5:

- not used in HOAPS (computation of additional fluxes and scaling parameters)

Step 6: Go to Main Loop

- The total transfer coefficient C_E (*Dalton number*) follows from Eq. 11.

	EUMETSAT SAF on CLIMATE MONITORING Algorithm Theoretical Basis Document HOAPS release 3.2	Doc.No.: SAF/CM/DWD/ATBD/HOAPS Issue: 1.1 Date: 25.03.2011
---	--	--

5.3.3 Assumptions and Limitations

While the COARE algorithm itself depends on some assumptions, the main limitations stem from the satellite retrieved input parameters wind speed, near surface specific humidity, and sea surface saturation specific humidity (derived from SST). Uncertainties in the retrieval procedures of these parameters are described in the relevant documents.

Due to the inability to derive the surface wind speed from SSM/I in cases of high atmospheric water content, i.e. precipitation, no values are retrieved for such situations.

Daily mean SST fields are used, which are calculated from AVHRR measurements. This may lead to errors in the flux estimates in certain regions with a strong diurnal cycle of the SST.

The COARE algorithms include a module to estimate the diurnal evolution of the oceanic warm layer. This part is disabled in the HOAPS retrieval, as it would require continuous radiative flux measurements for the whole day, which are neither available from the SSM/I nor the AVHRR.

As the implemented near-surface humidity retrieval is a statistical procedure (see section 5.1), it is only as good as the quality of the input data set. Since the training data for the retrieval originates from ship data, not all regions and hence atmospheric situations may be equally well represented in the training data set. This is for example the case for situations with relatively warm air layer above cold water, as it occurs in upwelling regions, where larger errors in the retrieval may occur. In scenes over very warm water masses with high air humidity the satellite-retrieved q_a signal tends to saturate. This leads to a tendency to underestimate q_a for values above 20 g/kg.



For the derivation of θ^* , the near surface air temperature is needed. Since it is not possible to measure this parameter directly from space, it is estimated using the mean of two simple bulk approaches:

- (a) The satellite derived near surface specific humidity is assumed to be at a constant relative humidity of 80% as proposed by Liu et al. (1994).
- (b) A constant temperature difference of 1 K between sea surface and air temperature is assumed (Wells and King-Hele, 1990).

On climatological scale these assumptions are valid for the majority of oceanic conditions. However, in regions with strong stable stratification of the atmospheric surface layer, this approach will affect the quality of sensible heat flux estimates. The impact of these assumptions on the latent heat flux retrieval is smaller since the air temperature is not directly used in the bulk formula and has only a secondary effect on the parameterization as it is used in the stability estimation of the atmosphere (Liu et al., 1994).

The COARE 2.6a/3.0 parameterizations are derived from flux measurements data containing situations with wind speeds in the range of 0-20 m/s. The accuracy described by Fairall (2003) is within 5% for wind speeds of 0–10 m/s and 10% for wind speeds between 10 and 20 m/s. For higher wind speeds the accuracy may decrease further.

Although the underlying data base has been extended for the recent versions of the COARE algorithm, most of the data stems from tropical regions of the pacific. However, there seem to be no implications for global application of the algorithm from this limitation as Brunke et. al. (2003) found the COARE algorithm to be one of the least problematic in a comparison of different bulk flux estimates over the tropical and midlatitude oceanic regions.

 	EUMETSAT SAF on CLIMATE MONITORING Algorithm Theoretical Basis Document HOAPS release 3.2	Doc.No.: SAF/CM/DWD/ATBD/HOAPS Issue: 1.1 Date: 25.03.2011
---	--	--

5.4 Precipitation (CM-144)

Microwave based retrievals of precipitation are based on the direct interaction of the radiation field and the hydrometeors (water droplets, ice particles). Emission from and scattering at cloud and rain particles increase the brightness temperatures at small frequencies and decrease the brightness temperatures at high frequencies relative to the radiometrically cold sea surface.

A neural network is used to derive a statistical retrieval for the precipitation from SSM/I brightness temperatures. The neural network was trained with precipitation rates retrieved from assimilated brightness temperatures in a 1D-Var scheme from the ECMWF. The resulting HOAPS precipitation retrieval is a statistical algorithm which only depends on SSM/I brightness temperatures as input and does not need first guess or other ancillary data.

5.4.1 Algorithm Description

Microwave based retrievals of precipitation are based on the direct interaction of the radiation field and the hydrometeors (water droplets, ice particles). In particular over the ocean the window channels of the SSM/I are well suited to detect precipitation. With the sea surface as a relatively homogeneous and radiometrically cold background, precipitating clouds systems are detectable by the emission signal of the hydrometeors and scattering of upwelling radiation at ice particles. (e.g. Liu and Curry, 1992, Weng and Grody, 1994)

The emission from clouds and liquid hydrometeor particles at low frequencies results in a strong contrast to the sea surface background and causes a strong increase of the brightness temperatures measured by the radiometer on the satellite.

The brightness temperatures at high frequencies show a strong decrease with increasing precipitation due to the scattering of radiation by frozen hydrometeors at the rain cloud top. A substantial attenuation of the ocean surface background signal occurs for high rain rates. These situations are mostly related to convective systems in which large amounts of ice particles are generated and transported to the cloud top.

These two nonlinear effects allow to derive precipitation algorithms for microwave radiometers, which can be either based on the scattering signal, the emission signal, or a combination of both.

5.4.2 Precipitation Neural Network Algorithm

Generally, the ocean surface precipitation algorithm relates an input vector P of the measured brightness temperatures to an output vector of the geophysical parameter(s) G through a transfer function f :

$$G = f(P) \quad (18)$$

where the transfer function is determined using a neural network in this case.

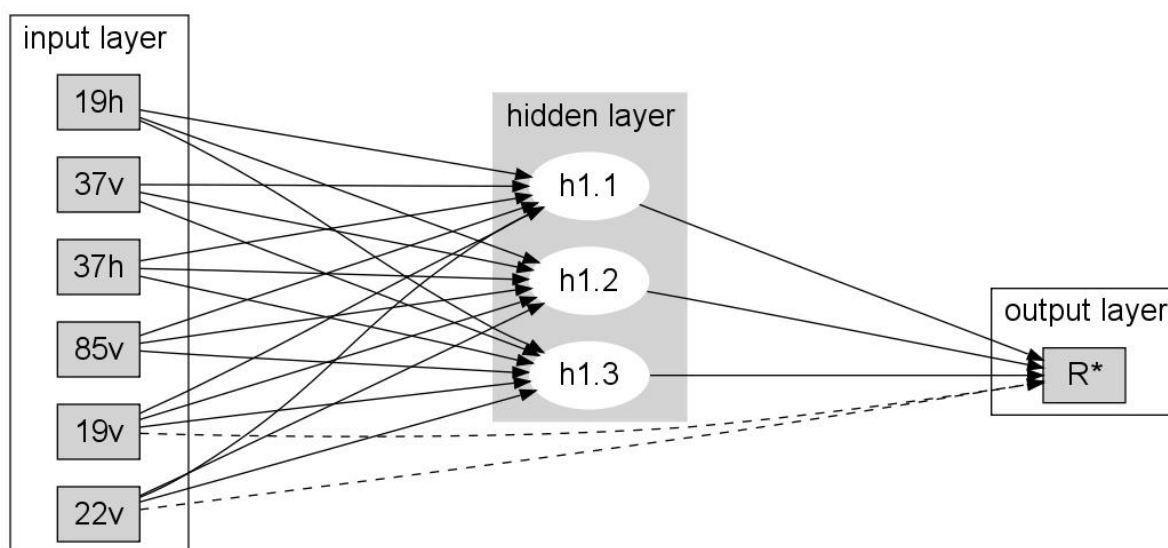


Figure 13: Neural network architecture of the precipitation retrieval algorithm.
(from Andersson et al., 2010)

For the precipitation algorithm a fully connected 3-layer feed forward network was constructed that includes:

- an input layer with six neurons at TB19v/h , TB22v , TB37v/h , and TB85v
- a hidden layer with three non-linear neurons using the tanh function as the activation function and
- an output layer with one linear neuron, the precipitation rate.
- additional direct linear connections from TB19v and TB22v to the output neuron

A schematic representation of the neural network architecture is shown in Figure 13.

The training data set for the neural network is based on radiative transfer calculations as described in Bauer et al. (2006a,b). The data set contains one month (August 2004) of assimilated SSM/I TBs and the corresponding ECMWF 1D-Var retrieved precipitation values of the European Centre for Medium-Range Weather Forecast (ECMWF) model.

Using precipitation values from the operational variational analysis to compile the training data set not only ensures the statistical representativeness of the input data, it also makes use of the advantage to have the background meteorological surface fields and profiles consistent with the measured SSM/I brightness temperatures. Moreover, it allows to construct a training data set from a large number of samples based on a sophisticated radiative transfer model.

This data set covers a wide variety of globally distributed rainfall events including extreme rainfall in hurricanes and snowfall at high latitudes. However, as it consists of more than 2.5 million data samples, it must be filtered in order to ensure good coverage and equal weight of all possible input TB combinations. Hence it was binned in a two-dimensional grid using TB22v and the polarization difference TB19v – TB19h as axis. The final training data set was then compiled by randomly taking an equal number of samples from each bin, which makes about 110,000 data samples in total of which only 50% were actually used for training. In order to avoid an inappropriately high influence of the larger uncertainties at higher

precipitation rates, the training values were scaled non-linearly by the following transformation, with R^* representing the transformed precipitation rate:

$$R^* = \sqrt{\log_{10}(R + 1)} \quad (19)$$

A lower threshold value is applied to the algorithm, below which the precipitation signal is considered to be zero. From experience with the formerly used algorithm, a value of 0.3 mm/h turned out to be an appropriate limit for distinguishing between a real precipitation signal and background noise.

The results of this training procedure are depicted in Table 2. The first line shows the quality of the derived algorithm compared to the unused second half of the training data set, the verification data set. Due to the strong peak of the distribution in case of low precipitation rates, the mean precipitation rate is only about 0.25 mm/h. The derived algorithm reproduces the test cases with a correlation of $r = 0.95$, a very small bias and a RMS of about 0.06 mm/h, which represents the theoretical algorithm accuracy. Testing the algorithm against the complete ECMWF data set yields a lower mean value of 0.16 mm/h, which is due to the larger sample size compared to the verification data, a bias of -0.06 mm/h, and a RMS of 0.16 mm/h. When a lower cutoff of 0.3 mm/h is applied to the ECMWF data set as it is done in the HOAPS retrieval, the mean precipitation rate increases to 0.78 mm/h. Bias and RMS are very low with values of -0.17 mm/d and 0.34 mm/h, respectively. The correlation is in the range of the two previous cases with $r = 0.91$.

The detection rates of the algorithm compared to the entire ECMWF data set are 93.4% correctness for the raining and rain-free cases, with a probability of rain detection of 70.5% and a false alarm rate of 20.4%.

Figure 14a shows the results of the training procedure as a comparison of the verification data set, which has not been used in the training procedure (see above), with the new neural network algorithm, the retrieval of Bauer and Schlüssel (1993) (HOAPS II), and the scattering algorithm of Ferraro (1997). As expected, the neural network performs significantly better in reproducing the rain rates of the verification data set compared to the other data sets. The Bauer algorithm exhibits a systematic underestimation of the precipitation. For rain rates exceeding 7 mm/h the neural network algorithm also exhibits an underestimation compared to the verification data set. The few cases with rain rates exceeding 12 mm/h in the verification data set are reproduced by the neural network and the Ferraro scattering algorithm with comparable values around 10 mm/h. The latter performs not well for lower rain rates due to the missing emission signal in the algorithm.

Figure 14b shows accumulated histograms of the rain rates derived with the three different precipitation algorithms on a logarithmic scale. The histogram bins represent the accumulated

Table 2: Accuracies of the neural net algorithm for precipitation. N = number of samples; mean, bias, and RMS are in mm/h. (see text)

Data set	N	Mean	Bias	RMS	R
Verification data set	54,850	0.255	-0.007	0.062	0.950
Complete data set	2,596,899	0.158	-0.063	0.157	0.915
Complete data set cutoff 0.3 mm/h	3,57,492	0.780	-0.166	0.342	0.907

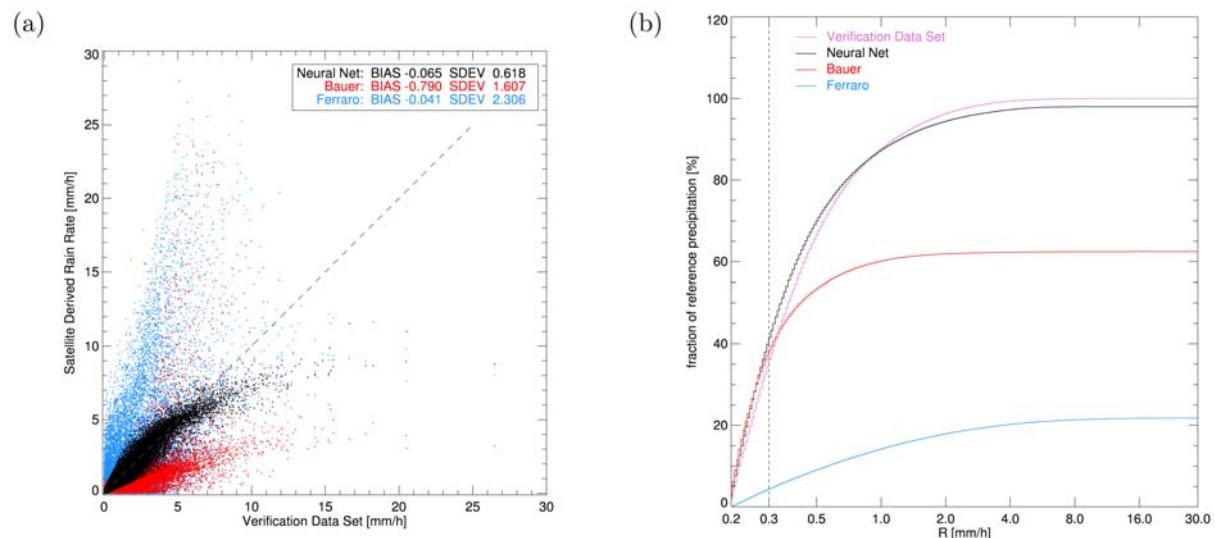


Figure 14: Comparison of different precipitation algorithms. (a) shows the retrieved precipitation rates of the neural network algorithm (black), the Bauer and Schlüssel (1993) algorithm (red) and the Ferraro (1997) algorithm (blue) against the precipitation rates from the verification data set. (b) shows the accumulated histogram of precipitation as the fraction of total precipitation for the different retrievals and the verification data set between 0.2 mm/h and 30 mm/h. (from Andersson, 2010)

fraction of the total reference precipitation from the verification data set in the range from 0.2 mm/h up to 30 mm/h. About 90% of the total ECMWF precipitation comes from rain rates up to 1 mm/h. The new neural network algorithm overestimates the rain rate below 0.3 mm/h and then slightly underestimates rain rates above 0.5 mm/h. This leads to a small underestimation of the total precipitation. Applying a lower threshold at 0.3 mm/h results in a total bias of -0.166 mm/h (Table 2).

5.4.3 Assumptions and Limitations



The neural network approach that is used for the precipitation here, resembles a statistical approximation of the input data set, which is in this case the physical ECMWF 1D-Var retrieval. Hence, the quality of a statistical retrieval strongly depends on the quality of the input data set.

Here the well established ECMWF radiative transfer and assimilation schemes are used to generate the input data set. However, a complete validation of precipitation data over the ocean is nearly impossible. This accounts for both, the training data as well as for the derived satellite retrieval.

Another point is the representativeness of the training data for all kinds of different atmospheric situations and surface conditions. This requirement is likely fulfilled by the training data set as it contains more than 50,000 globally distributed data samples.

Another general limitation of the retrieval is the detectability of precipitation at low rain rates. The current retrieval uses a lower cutoff value of 0.3 mm/h. Hence, these light rain events are not captured by the retrieval.

Further information on the accuracy of the precipitation parameter are given in the validation Report [RD 3].

 	EUMETSAT SAF on CLIMATE MONITORING Algorithm Theoretical Basis Document HOAPS release 3.2	Doc.No.: SAF/CM/DWD/ATBD/HOAPS Issue: 1.1 Date: 25.03.2011
---	--	--

5.5 Freshwater flux (CM-146)

The ocean surface freshwater flux is computed as the difference of evaporation minus precipitation. Hence, the product relies on the output of the individual HOAPS algorithms, see section 5.3 and 5.4 for details. The freshwater flux at the sea surface is defined as positive for a flux that is directed from the ocean into the atmosphere.

The freshwater flux product is not computed directly from the SSM/I swath data, since the concurrent retrieval of precipitation and evaporation is not possible for the most cases with precipitation.

In order to retrieve the freshwater flux, the input parameters precipitation and evaporation are averaged separately. Then the freshwater flux is computed for the gridded data products for each grid box as the difference between the spatial and temporal means of evaporation and precipitation.

In certain regions with frequent precipitation this method may introduce a slight clear sky bias from the evaporation fields in the resulting freshwater flux fields (see section 5.5.1).


Due to the method of calculating the freshwater flux from the mean evaporation and precipitation fields, no statistical variables like the number of observations or standard deviation are available in the gridded freshwater flux data products.

5.5.1 Assumptions and Limitations

Since it is not possible to retrieve the evaporation in situation with precipitation (except for light rain), the freshwater flux cannot be determined for individual SSM/I pixels in these cases. Hence it is computed for each grid box as the difference of the spatially and temporally averaged evaporation and precipitation fields. These averages may contain different numbers of observations, as the evaporation is not retrieved for precipitating cases. The largest effect on the mean freshwater flux fields by this clear sky bias is observed over the Southern Ocean, the ITCZ, where in 10% to 15% of all SSM/I observations the retrieval of wind speed, near surface humidity, and hence evaporation is not possible.


The systematic omission of potentially extreme deviations from the mean values or from the surrounding area may result in unintended biases. However, even under the extreme assumption of 100% error for the missed evaporation estimates, this would not result in more than about 10-15% error for the monthly mean in the most affected regions (see also Validation Report RD 3).

Since the mean values of the input parameters, evaporation and precipitation are often of the same order of magnitude, the resulting values in the freshwater flux fields are sensitive to relatively small variations in either of the input parameters. Small errors in one of the input parameters may lead to larger deviations in the resulting freshwater flux fields. This effect reduces with longer temporal and/or larger spatial averages.


	EUMETSAT SAF on CLIMATE MONITORING Algorithm Theoretical Basis Document HOAPS release 3.2	Doc.No.: SAF/CM/DWD/ATBD/HOAPS Issue: 1.1 Date: 25.03.2011
---	--	--

6 References



- Andersson, A., Fennig, K., Klepp, C., Bakan, S., Graßl, H., and Schulz, J.: The Hamburg Ocean Atmosphere Parameters and Fluxes from Satellite Data – HOAPS-3, *Earth Syst. Sci. Data*, 2, 215–234, doi:10.5194/essd-2-215-2010, 2010.
- Ataktürk, S. S., and K. B. Katsaros: Estimates of surface humidity and wind speed obtained from satellite data in the stratocumulus regime in the Azores region. *Remote Sensing of the Pacific Ocean by Satellites*, R. A. Brown, Ed., Southwood Press, 16–22, 1998
- Bauer, P.: Over-ocean Rainfall Retrieval from Multisensor Data of the Tropical Rainfall Measuring Mission. Part I: Design and Evaluation of Inversion Databases, *J. Atmos. Oceanic Technol.*, 18, 1315–1330, 2001.
- Bauer, P., Lopez, P., Benedetti, A., Salmond, D., and Moreau, E.: Implementation of 1D+4D-Var Assimilation of Precipitation-affected Microwave Radiances at ECMWF. I: 1D-Var, *Q. J. Roy. Meteor. Soc.*, 132, 2277–2306, 2006a.
- Bauer, P., Moreau, E., Chevallier, F., and O’Keeffe, U.: Multiple-scattering Microwave Radiative Transfer for Data Assimilation Applications, *Q. J. Roy. Meteor. Soc.*, 132, 1259–1281, 2006b.
- Bentamy, A., Katsaros, K. B., Mestas-Nunez, A. M., Drennan, W. M., Forde, E. B., and Roquet, H.: Satellite Estimates of Wind Speed and Latent Heat Flux Over the Global Oceans, *J. Climate*, 16, 637–656, 2003.
- Bradley, E. F., Fairall, C. W., Hare, J. E., and Grachev, A. A.: An Old and Improved Bulk Algorithm for Air-sea Fluxes: COARE 2.6 A, in: *Preprints, 14th Symp. on Boundary Layers and Turbulence*, Aspen, CO, Am. Meteorol. Soc., 294–296, 2000
- Brunke, M. A., C. W. Fairall, X. Zeng, L. Eymard, and J.A. Curry: Which bulk aerodynamic algorithms are least problematic in computing ocean surface turbulent fluxes? *J. Climate*, 16, 619–635, 2003
- Casey, K. S.: Global AVHRR 4 km SST for 1985–2001, Pathfinder V5.0, NODC/RSMAS, Tech. Rep., NOAA National Oceanographic Data Center, Silver Spring, Maryland, NODC Accession Numbers 0001763–0001864: Pathfinder AVHRR Version 5.0, 2004.
- Colton, M. C. and Poe, G. A.: Intersensor Calibration of DMSP SSM/I’s: F-8 to F-14, 1987–1997, *IEEE Trans. Geosci. Remote Sens.*, 37, 418–439, 1999.
- Edson, J. B., C. W. Fairall, S. E. Larsen, and P. G. Mestayer: A study of the inertial-dissipation technique for computing air-sea fluxes. *J. Geophys. Res.*, 96, 10689–10711, 1991
- Fairall, C. W. and Larsen, S. E.: Inertial-dissipation methods and turbulent fluxes at the air-ocean interface, *Boundary-Layer Meteor.*, 34, 287–301, 1986
- Fairall, C. W., E. F. Bradley, D. P. Rogers, J. B. Edson, and G. S. Young, 1996: Bulk Parameterization of Air–sea Fluxes for Tropical Ocean–Global Atmosphere Coupled Ocean–Atmosphere Response Experiment. *J. Geophys. Res.*, 101, 3747–3764, 1996

	EUMETSAT SAF on CLIMATE MONITORING Algorithm Theoretical Basis Document HOAPS release 3.2	Doc.No.: SAF/CM/DWD/ATBD/HOAPS Issue: 1.1 Date: 25.03.2011
---	--	--

- Fairall, C. W., A. B. White, J. B. Edson, and J. E. Hare: Integrated shipboard measurements of the marine boundary layer. *J. Atmos. Oceanic Technol.*, 14, 338-359., 1997
- Fairall, C. W., Bradley, E. F., Hare, J. E., Grachev, A. A., and Edson, J. B.: Bulk parameterization of Air-sea Fluxes: Updates and Verification for the COARE Algorithm, *J. Climate*, 16, 571–591, 2003.
- Ferraro, R.: Special sensor microwave imager derived global rainfall estimates for climatological applications, *J. Geophys. Res.*, 102, 16715–16735, 1997.
- Furhop, R. and Simmer, C.: SSM/I Brightness Temperature Corrections for Incidence Angle Variations, *J. Atmos. Oceanic Technol.*, 13, 246–254, 1996.
- GLOBE Task Team: The Global Land One-kilometer Base Elevation (GLOBE) Digital Elevation Model, Version 1.0., Tech. Rep., National Oceanic and Atmospheric Administration, National Geophysical Data Center, 325 Broadway, Boulder, Colorado 80303, USA, <http://www.ngdc.noaa.gov/mgg/topo/globe.html>, 1999.
- Goodberlet, M., Swift, C., and Wilkerson, J.: Remote sensing of ocean surface winds with the Special Sensor Microwave/Imager, *J. Geophys. Res.*, 94, 14547–14555, 1989.
- Harries, J. and Fytian, J.: On the stability of the Earth's radiative energy balance: Response to the Mt. Pinatubo eruption, *Geophys. Res. Lett.*, 33, doi:10.1029/2006GL027457, L23814, 2006.
- Hollinger, J. P., Peirce, J. L., and Poe, G. A.: SSM/I Instrument Evaluation, *IEEE Trans. Geosci. Remote Sens.*, 28, 781–790, 1990.
- Kilpatrick, K. A., Podesta, G. P., and Evans, R.: Overview of the NOAA/NASA Advanced Very High Resolution Radiometer Pathfinder Algorithm for Sea Surface Temperature and Associated Matchup Database, *J. Geophys. Res.-Oceans*, 106, 9179–9197, 2001.
- Krasnopolsky, V. M., Breaker, L. C., and Gemmil, W. H.: A Neural Network as a Nonlinear Transfer Function Model for Retrieving Surface Wind Speeds from the Special Sensor Microwave Imager, *J. Geophys. Res.-Oceans*, 100, 11033–11045, 1995.
- Liu, W. T.: Statistical Relation between Monthly Mean Precipitable Water and Surface-Level Humidity over Global Oceans. *Mon. Wea. Rev.*, 114, 1591–1602, 1986
- Liu, W., Zhang, A., and Bishop, J.: Evaporation and solar irradiance as regulators of sea surface temperature in annual and interannual changes, *J. Geophys. Res.*, 99, 12623–12638, 1994
- Liu, G., and J. A. Curry: Retrieval of Precipitation From Satellite Microwave Measurement Using Both Emission and Scattering, *J. Geophys. Res.*, 97(D9), 9959–9974, doi:10.1029/92JD00289, 1992
- NODC: 4 km Pathfinder Version 5.0 User Guide, National Oceanographic Data Center, Silver Spring, Maryland, <http://www.nodc.noaa.gov/sog/pathfinder4km/userguide.html> (last access: April 2010), 2008.

	EUMETSAT SAF on CLIMATE MONITORING Algorithm Theoretical Basis Document HOAPS release 3.2	Doc.No.: SAF/CM/DWD/ATBD/HOAPS Issue: 1.1 Date: 25.03.2011
---	--	--



- Reynolds, R. W.: Impact of Mount Pinatubo Aerosols on Satellite-derived Sea Surface Temperatures, *J. Climate*, 6, 768–774, 1993.
- Reynolds, R. W., Rayner, N. A., Smith, T. M., Stokes, D. C., and Wang, W.: An Improved In Situ and Satellite SST Analysis for Climate, *J. Climate*, 15, 1609–1625, doi:10.1175/1520-0442(2002)015 1609:AIISAS 2.0.CO;2, 2002.
- Ritchie, A. A., Smith, M. R., Goodman, H. M., Schudalla, R. L., Conway, D. K., LaFontaine, F. J., Moss, D., and Motta, B.: Critical Analyses of Data Differences Between FNMOC and AFGWC Spawned SSM/I Datasets, *J. Atmos. Sci.*, 55, 1601–1612, 1998.
- Schlüssel, P., Satellite – derived low level atmospheric water vapour content from synergy of AVHRR with HIRS. *Int. J. Remote Sens.* 10, 705–721, 1989
- Schlüssel, P. and Emery, W. J.: Atmospheric Water-vapor Over Oceans from SSM/I Measurements, *Int. J. Remote Sens.*, 11, 753–766, 1990.
- Schlüssel, P. and Luthardt, H.: Surface Wind Speeds Over the North Sea from Special Sensor Microwave/Imager (SSM/I) Observations, *J. Geophys. Res.-Oceans*, 96, 4845–4853, 1991.
- Schlüssel, P.: Passive Fernerkundung der unteren Atmosphäre und der Meeresoberfläche aus dem Weltraum, Vol. 20, Berichte aus dem Zentrum für Meeres- und Klimaforschung, Reihe A: Meteorologie, Max Planck Institute for Meteorology, Bundesstr. 55, 20146 Hamburg, Germany, ISSN 0947-7128, 1995.
- Schulz, J., Schlüssel, P., and Graßl, H.: Water-vapor in the Atmospheric Boundary Layer over Oceans from SSM/I Measurements, *Int. J. Remote Sens.*, 14, 2773–2789, 1993.
- Smith, S. D., C. W. Fairall, G. L. Geernaert, and L. Hasse: Air–seafluxes: 25 years of progress. *Bound.-Layer Meteor.*, 78, 247–290, 1996.
- Soden, B., Wetherald, R., Stenchikov, G., and Robock, A.: Global cooling after the eruption of Mount Pinatubo: A test of climate feedback by water vapor, *Science*, 296, 727–730, 2002.
- Spencer, R. W., Goodman, H. M., and Hood, R. E.: Precipitation Retrieval over Land and Ocean with the SSM/I: Identification and Characteristics of the Scattering Signal, *J. Atmos. Oceanic Technol.*, 6, 254–273, doi:10.1175/1520-0426(1989)006 0254:PROLAO 2.0.CO;2, 1989.
- Stogryn, A., Butler, C., and Bartolac, T.: Ocean surface wind retrievals from special sensor microwave imager data with neural networks, *J. Geophys. Res.*, 99, 981–984, 1994.
- Swift, C. T., Fedor, L. S., and Ramseier, R. O.: An Algorithm to Measure Sea Ice Concentration with Microwave Radiometers, *J. Geophys. Res.-Oceans*, 90, 1087–1099, 1985.
- Trenberth, Kevin E., John T. Fasullo, Jeffrey Kiehl: Earth's Global Energy Budget. *Bull. Amer. Meteor. Soc.*, 90, 311–323, 2009.

 	EUMETSAT SAF on CLIMATE MONITORING Algorithm Theoretical Basis Document HOAPS release 3.2	Doc.No.: SAF/CM/DWD/ATBD/HOAPS Issue: 1.1 Date: 25.03.2011
---	--	--

- Webster Jr., W. J., Wilheit, T. T., Ross, D. B., and Gloersen, P.: Spectral Characteristics of the Microwave Emission From a Wind-Driven Foam-Covered Sea, *J. Geophys. Res.*, 81, 3095–3099, doi:10.1029/JC081i018p03095, 1976.
- Wells, N. and King-Hele, S.: Parametrization of tropical ocean heat flux, *Q. J. Roy. Meteor. Soc.*, 116, 1213–1224, 1990
- Weng, F., and N. C. Grody: Retrieval of cloud liquid water using the special sensor microwave imager (SSM/I), *J. Geophys. Res.*, 99(D12), 25,535–25,551, doi:10.1029/94JD02304, 1994.
- Wentz, F. J.: User’s Manual for SSM/I Antenna Temperature Tapes Revision 1, Technical Report 120191, Remote Sensing Systems, Santa Rosa, California, 1991.
- Wentz, F. J.: Production of SSM/I Data Sets, Technical Report 90192, Remote Sensing Systems, Huntsville, Alabama, 1992.
- Winterfeldt, J., Andersson, A., Klepp, C., Bakan, S., and Weisse, R.: Comparison of HOAPS, QuikSCAT and buoy wind speed in the eastern North Atlantic and the North Sea, *IEEE Trans. Geosci. Remote Sens.*, 48, 338–348, doi:10.1109/TGRS.2009.2023982, 2010.

7 Glossary

ATBD	Algorithm Theoretical Baseline Document
ATT	Antenna Temperature Tapes
AVHRR	Advanced Very High Resolution Radiometer
CDOP	Continuous Development and Operations Phase
CM SAF	Satellite Application Facility on Climate Monitoring
COADS	Comprehensive Ocean-Atmosphere Data Set
COARE	Coupled Ocean Atmosphere Response Experiment
DMSP	Defense Meteorological Satellite Program
DRI	Delivery Readiness Inspection
DWD	Deutscher Wetterdienst (German MetService)
ECMWF	European Centre for Medium Range Forecast
ECV	Essential Climate Variable
EPS	European Polar System
EUMETSAT	European Organisation for the Exploitation of Meteorological Satellites
FMI	Finnish Meteorological Institute
FOV	Field of view
GCOS	Global Climate Observing System
GLOBE	The Global Land One-kilometer Base Elevation
HOAPS-C	HOAPS Composite product
HOAPS-G	HOAPS Gridded product
HOAPS-S	HOAPS Scan product
HOAPS	The Hamburg Ocean Atmosphere Fluxes and Parameters from Satellite data
IOP	Initial Operations Phase
ITCZ	Inter-Tropical Convergence Zone
KNMI	Koninklijk Nederlands Meteorologisch Instituut
MOST	Monin-Obukhov similarity theory
MSG	Meteosat Second Generation
NASA	National Aeronautics and Space Administration
NCEP	National Centers for Environmental Prediction
NDBC	National Data Buoy Center
NESDIS	National Environmental Satellite, Data, and Information System
NOAA	National Oceanic & Atmospheric Administration

 	EUMETSAT SAF on CLIMATE MONITORING Algorithm Theoretical Basis Document HOAPS release 3.2	Doc.No.: SAF/CM/DWD/ATBD/HOAPS Issue: 1.1 Date: 25.03.2011
---	--	--

NODC	National Oceanographic Data Center
NWP	Numerical Weather Prediction
PRD	Product Requirement Document
PUM	Product User Manual
RMIB	Royal Meteorological Institute of Belgium
RMS	Root Mean Square
RSMAS	Rosenstiel School of Marine and Atmospheric Science
RSS	Remote Sensing Systems
SAF	Satellite Application Facility
SMHI	Swedish Meteorological and Hydrological Institute
SSM/I	Special Sensor Microwave Imager
SSMIS	Special Sensor Microwave Imager Sounder
SST	Sea Surface Temperature
TAO	Tropical Atmosphere/Ocean project
TDR	Temperature Data Records